Electronic-structure methods for twisted moiré layers

Stephen Carr[1] ✉, *Shiang Fang*[1] *and Efthimios Kaxiras*[1,2] ✉

Abstract | When single layers of 2D materials are stacked on top of one another with a small twist in orientation, the resulting structure often involves incommensurate moiré patterns. In these patterns, the loss of angstrom-scale periodicity poses a significant theoretical challenge, and the new moiré length scale leads to emergent physical phenomena. The range of physics arising from twisted bilayers has led to significant advances that are shaping into a new field, twistronics. At the moiré scale, the large number of atoms in these systems can make their accurate simulation daunting, necessitating the development of efficient multiscale methods. In this Review, we summarize and compare such modelling methods — focusing in particular on density functional theory, tight-binding Hamiltonians and continuum models — and provide examples spanning a broad range of materials and geometries.

When two single layers of a 2D material are stacked on top of each other with a small misalignment (such as a twist, FIG. 1), they produce a moiré pattern of much larger length scale than the periodicity of each layer (FIG. 1a). The pattern is more often than not an incommensurate structure and produces twist-dependent emergent electronic behaviour (FIG. 1c). A case in point is the appearance of correlated phases in twisted bilayer graphene (TBG)[1,2]. The observed strong correlations are caused, in part, by a flattening of the bands near the Fermi energy that only occurs if the twist angle is near the magic angle of 1.1° (FIG. 1b,e). The twist angle controls the energy scale at which the Dirac cones of the two graphene layers intersect in momentum space. When this energy scale is comparable to the interlayer coupling energy, band hybridization induces flat bands, as first pointed out by Rafi Bistritzer and Allan MacDonald[3]. The flat bands have an energy width of only a few meV, and, so, electron–electron interactions can dominate the band structure and give rise to correlated phenomena, a rarity for graphene devices. At extremely small twist angles, when the moiré length scale is on the order of 100 nm, 1D features appear in the relaxed atomic structure[4,5], introducing 1D electronic modes[6–9] (FIG. 1d). Even when the length scale is only a few nanometres, the transport and optical and mechanical properties of these structures are controllable by manipulating the twist angle[10–17].

Experiments have mostly focused on graphitic twisted systems, but moiré bilayers of other semiconducting and metallic materials are being explored. Surveys of crystal-structure databases predict over 1,000 candidates for unique 2D van der Waals materials[18–20], suggesting millions of possibilities for twisted bilayer systems. To facilitate the exploration of this vast space of possible structures, theory is called upon to provide accurate and robust predictions of the most interesting choices. Towards this goal, we provide, in this Review, a summary of existing modelling techniques for single-particle electronic structure in moiré heterostructures. Although our focus is electronic behaviour (band structures, transport, optical properties), we also introduce and discuss atomistic relaxation, which plays an important role in determining the electronic structure.

As a first step, we cover the popular 2D materials used in moiré physics (FIG. 2), the common conventions and vocabulary for twistronics and the 'control knobs' that are available for tuning the electronic structure in moiré bilayers. The remainder of the Review is split into two sections, atomistic modelling and continuum modelling. Atomistic models, such as density functional theory (DFT) and tight-binding Hamiltonians, allow for a natural inclusion of both the small length scale of the primitive unit cells and the large length scale of the moiré pattern. Continuum models integrate out the small length scale, capturing emergent physics by considering only the moiré length scale. Both approaches have advantages and disadvantages, and the salient characteristics of various models are compared in the conclusion.

Moiré materials

Hexagonal boron nitride (hBN) is commonly used in experiments involving 2D materials because of its easy exfoliation and large band gap. Being electronically and mechanically inert, it makes an ideal substrate for

[1]*Present address: Department of Physics, Harvard University, Cambridge, MA, USA.*

[2]*John A. Paulson School of Engineering and Applied Sciences, Harvard University, Cambridge, MA, USA.*

✉*e-mail: stephen_carr1@brown.edu; kaxiras@physics.harvard.edu*

https://doi.org/10.1038/s41578-020-0214-0

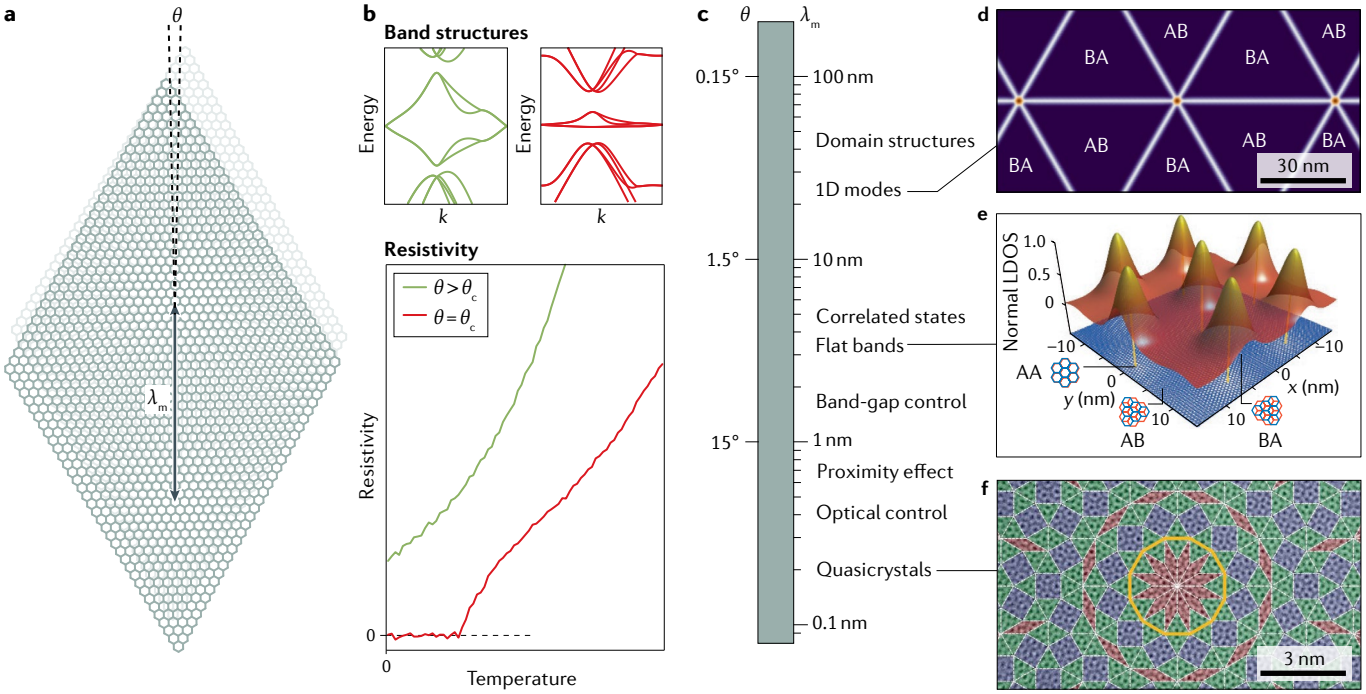

Fig. 1 | **An introduction to twistronics. a** | A bilayer with a relative twist angle θ. The moiré length λ_m is indicated by the double-headed arrow and describes the periodicity of the interference pattern between the misaligned layers. **b** | The electronic properties of a twisted bilayer can depend sensitively on the twist angle θ: by decreasing the angle in twisted bilayer graphene (TBG), the normally dispersive bands ($\theta > \theta_c$, green) corresponding to normal conductivity become very flat ($\theta = \theta_c$, red), corresponding to a superconducting behaviour. This phase transition occurs near a critical twist angle, $\theta_c \approx 1.1°$. **c** | By controlling θ, the value of λ_m can change from a few angstroms to hundreds of nanometres. Unique physics can be found throughout this range of length scales. **d** | At very small twist angles (large λ_m), atomic reconstruction forms domain-wall structures and helps define 1D electronic modes (simulation of TBG). **e** | For TBG and many semiconductors, flat bands appear in the electronic structure when λ_m is near 10 nm, causing electron confinement and correlation effects associated with specific stacking orders. **f** | At large twist angles (small λ_m), the electronic structure is still highly tunable: when λ_m is close to the size of the crystal lattice, quasicrystals can emerge. LDOS, local density of states. Panel **d** adapted with permission from REF.[97], APS. Panel **e** adapted from REF.[1], Springer Nature Limited. Panel **f** reprinted with permission from REF.[55], AAAS.

many transport, optical and electron-beam experiments. Owing to a mismatch of roughly 2% in lattice constants, a graphene layer aligned on hBN is a useful platform for studying moiré physics[21–32]. It enabled an important early example of an electronic moiré experiment[33–35], in which the large length scale was used to observe Hofstadter's butterfly pattern[36] at realistic magnetic fields. Recent experiments have found correlated phenomena in superlattices of trilayer graphene on hBN[37,38], similar to those observed in TBG. Unlike twisted bilayers of the same material, the inherent lattice mismatch between graphene and hBN limits the maximum moiré length. Several proposals have pushed the envelope of complicated graphene/hBN heterostructures, including interference between two independently twisted hBN/graphene interfaces[39], twisted hBN bilayers[40] and devices with in situ control of the twist angle[12,13].

In terms of pure graphitic devices, TBG has received the most attention[1–3,41–43] The first logical extension is to replace one of the monolayers with a Bernal stacked bilayer, resulting in a twisted heterostructure that can still exhibit flat-band physics[44,45]. Another choice is a twisted bilayer of Bernal stacked graphene bilayers, often called the twisted double bilayer, which was recently observed to host strong correlations and superconductivity[46–51]. A categorization of graphene-based devices with a single twist angle has been performed from different perspectives, classifying the types of flat bands and topological bands that can occur[52–54]. When the graphene bilayer is twisted at 30°, it forms a robust quasicrystal[55,56] (FIG. 1f). Another structure of interest is the doubly incommensurate graphene trilayer, in which the second and third layers are independently rotated relative to the first[57,58]. Such devices create complicated moiré patterns and additional van Hove singularities in the graphene density of states[45,59]. There have also been investigations of systems with alternating twist[60,61] or with consistent twist between infinite layers[62]. All studies of twisted graphene layers show band-flattening effects of various kinds. Even by constraining our options to just one type of 2D material, in this case, graphene, there is still a dizzying amount of possibilities in terms of multilayers with a twist.

Although graphene-based heterostructures are the most popular choice for device fabrication, another family of materials that has seen growing interest as a platform for moiré physics is transition-metal dichalcogenides (TMDCs)[39,51,63–65]. TMDCs include metallic and semiconducting materials, with a triangular lattice

geometry that can host both hexagonal (2H) and tetragonal (1T) bulk phases[66,67] that differ in the coordination of the chalcogenides around the central metal atom. The electronic structure and geometry varies as one chooses different metal or chalcogenide elements[68–70], giving additional control over the electronic and mechanical properties in these systems. Many of these materials have superconducting and charge-density wave phases even in their bulk form, but the critical temperatures depend strongly on the number of layers[71,72]. The local stacking order in TMDCs has a noticeable effect on optical properties[73]. When two layers with lattice mismatch are grown on top of one another, the resulting moiré pattern can cause modulations in the electronic band structure, such as a spatially dependent band gap[74] or twist-controlled interlayer excitons[75–77]. Bilayers with long moiré lengths are predicted to lead to quasiparticle localization[78–80] and may have non-trivial topological character[81].

Finally, there are magnetic van der Waals materials, with CrI_3 being the best known example. This class of materials has a stacking-dependent magnetic order[82,83], which, when combined with a twist angle, may allow for uniform domains of antiferromagnetic and ferromagnetic order.

This is a sampling of the most common materials used in moiré research (FIG. 2), but this short Review does not exhaust the possible structures[84]. For the interested reader, there are libraries of possible 2D materials containing thousands of entries that have been generated from screening studies of crystallographic databases[18–20].

Moiré geometry

When a 2D crystal is twisted relative to another, there is no guarantee of periodicity in the resulting atomic structure. The two crystal lattices 'beat' in space, giving rise to a 2D moiré pattern defined by the interference between the two layers' individual periodicities (FIG. 1a). For some special angles, a translational symmetry is retained, but its length scale is much larger than the original unit cells of the crystals. This is the case for a commensurate twist angle, and the retained symmetry defines the commensurate moiré supercell. When no such translational symmetry is retained, the system is incommensurate.

Even in the incommensurate case, there is still a well-defined moiré length scale, λ_m, for the twisted bilayer. For twisted triangular lattices, the law of cosines yields $\lambda_m(\theta) = (a/2)/\sin(\theta/2)$, where a is the lattice constant of the constituent monolayer and θ is the twist angle. This length scale can be interpreted as an approximate periodicity in the local arrangement between the layers' unit cells and is the distance between the light stacking spots of the twisted hexagonal bilayer in FIG. 1a. Although we focus here on twisted heterostructures of the same lattice constant, the case of materials with slight lattice mismatch is similar and is discussed when relevant. In those cases, λ_m has a more complicated form and, generally, small lattice strain is required to create commensurate supercells[85,86]. Given a lattice mismatch of δ, the moiré length is given by

$$\lambda_m(\theta,\delta) = \frac{(1+\delta)a}{\sqrt{2(1+\delta)(1-\cos\theta)+\delta^2}}. \quad (1)$$

This expression is derived by considering the difference between the two layers' reciprocal lattice vectors (see the supplementary information of REF.[22]).

In real devices, the twist angle cannot be controlled as precisely as in simulations. Recent reports put the state-of-the-art experimental control of the angle near 0.1° (REF.[87]), but this comes with a caveat. The current stacking methods usually require breaking a monolayer into two parts and then placing one part on top of the other. This technique, named the tear-and-stack approach[88], can introduce huge amounts of mechanical strain and non-uniformity in the moiré heterostructure.

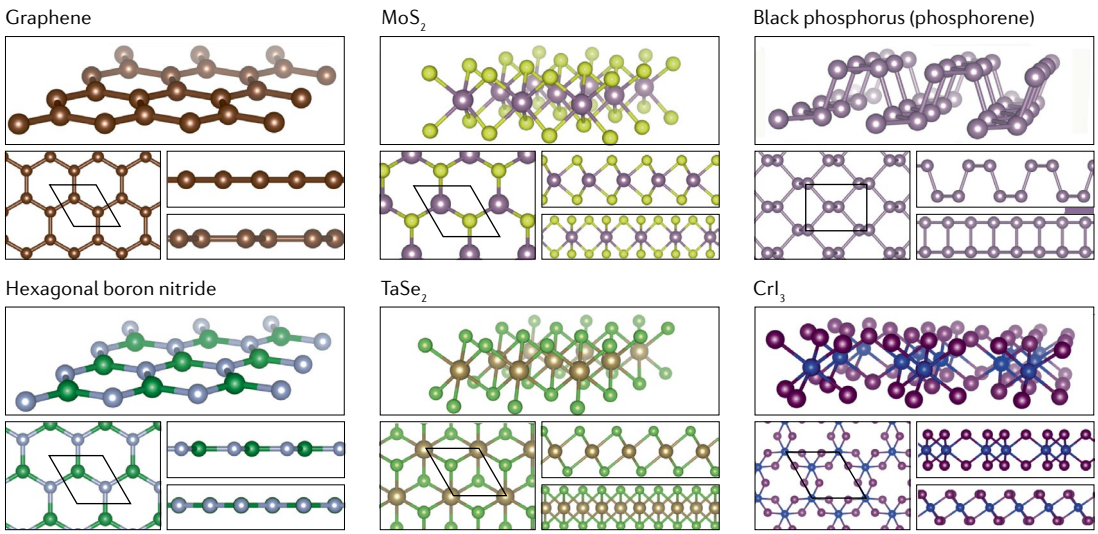

Fig. 2 | **Examples of 2D materials.** Crystal structures of graphene, hexagonal boron nitride, the 2H (hexagonal) phase of MoS_2, the 1T (tetragonal) phase of $TaSe_2$, black phosphorus (phosphorene) and the magnetic material CrI_3. For each material, we show a perspective view, accompanied by a top-down view along the normal to the plane $\hat{z}$ and two side views, along $\hat{x}$ and $\hat{y}$.

In particular, the twist angle is often non-uniform in space[5,43,89]. Experimental results on the electronic structure of these materials rely on devices with a high degree of spatial uniformity, which are often fabricated with great effort due to this technique's low yield of high-quality devices.

When discussing moiré heterostructures, the term 'bilayer' is often misused. It implies that the system has two constituent layers, each an ideal 2D crystalline structure with its own short-range translational symmetry of a few angstroms. However, the 'layer' does not need to be just a single sheet of a van der Waals material. For example, a layer could be a collection of tens of nanometres of Bernal stacked graphite[42,90]. When the two layers are not identical, the system can be referred to more generally as a heterostructure, or a heterobilayer. When the two layers are identical, it is a bilayer but is sometimes called a homobilayer to differentiate it from the previous case. More complicated structures with a single twist angle can also be considered, such as a three-sheet graphene system in which the top and bottom sheets form one effective layer and the middle sheet another, with a relative twist angle between the two[60,61]. A unified naming scheme is still needed for this emerging class of materials. For now, they are described self-consistently within each individual work. Here, we use the term bilayer for a system with a single unique moiré interface and reserve 'trilayer' or 'multilayer' for systems with more than one moiré interface (for example, three sheets of graphene, each at a different relative twist angle to the others[57–59]).

Local stacking order

Moving the axis of rotation to a different point on the bilayer is equivalent to choosing a different initial in-plane displacement between the layers. After a rotation, the local displacement between the unit cells of each layer varies in space (FIG. 3a). This variation captures another important aspect of moiré systems and is referred to by many names in the literature: local stacking order, atomic disregistry, shift, alignment and more. Because the two lattices are no longer identical after twisting, there is always a spatial variation in this local stacking order. For a commensurate system, only a finite set of local stackings occur, but for an incommensurate system, all possible stackings occur[91], and each stacking has a one-to-one correspondence with a unique location in space[92].

Local stackings that admit high-symmetry point groups often correspond to the critical points of stacking-dependent electronic properties. The labelling of the high-symmetry stackings varies by material family. They are usually related to a bulk phase and can inherit a specific name based on the naming convention used in studies of the bulk system. For graphene bilayers, AA and AB stacking refer to regions where two or one carbon atoms, respectively, are eclipsed by a carbon of the opposite layer in each unit cell. The AB configuration is called Bernal stacking after the discoverer of the crystallographic structure of bulk graphite[93]. In TMDCs, the AB and BA labels often refer to the orientation of the two layers rather than to their local stacking (FIG. 3b,c). Other naming conventions are used for the local stackings in TMDCs but there is not yet a uniform standard.

In a twisted system, the local configuration, $\boldsymbol{d}$, is a function of space, $\boldsymbol{d}(\boldsymbol{r})$. The electronic properties calculated from the untwisted reference stackings can be leveraged to approximate the twisted bilayer with a smoothly varying field over the moiré pattern. This is the basis of most continuum descriptions of these systems, which can accurately capture atomic relaxations[31,94–97] and electronic phenomena[3,9,41,78,81,98–102]. These models are described in the section on continuum modelling.

Control knobs

The degree of control in moiré systems can be compared with that available in other artificial lattices, such as optical lattices[103], with moiré systems having a smaller length scale (nanometres instead of micrometres). An alternative approach to the use of twist angles for generating a periodic potential on a 2D system is the use of patterned metallic gates on the surface of the material[104,105]. Unlike in a twisted interface, the strength and shape of these potentials can be directly controlled, but defects and irregularities are more easily introduced during fabrication.

For moiré systems with a single twist angle, it is useful to visualize the electronic Hamiltonian as divided into three parts: two periodic Hamiltonians, H_1 and H_2, and an interlayer coupling Hamiltonian, T. The H_i have the periodicity of a conventional 2D lattice, of order angstrom, whereas T captures the periodicity of the superlattice. The length scale of this interlayer periodicity, λ_m, is proportional to $1/\theta$. This provides an unprecedented amount of control on the moiré interface, allowing for the creation of systems with length scales anywhere between 1 and 100 nm (FIG. 1c), controllable at the time of fabrication.

External pressure can reduce the distance between layers, increasing the strength of the interlayer coupling, $T(\boldsymbol{r})$. This effect was first predicted in TBG with DFT-based multiscale calculations[106,107] and, soon thereafter, verified in experiments as a pressure dependence of the magic angle[43]. A similar theoretical study has also been performed on the twisted double-bilayer graphene system[50]. Although the study of moiré devices under pressure is challenging, pressure is likely to mature as an important tool for tuning electronic structure in moiré heterostructures.

Another unique advantage of using an artificial superlattice in a 2D solid-state device is the access it provides to powerful phase-altering perturbations in the Hamiltonian. The most common perturbations are electromagnetic fields[7,50,108] and external strain forces[109–112]. The electronic structure can also be greatly modified with the use of chemical intercalation of charged ions between layers[32,113–116] and targeted defect formation[117,118].

Atomistic modelling

The most direct way to model any crystalline system is to consider the local electronic environment near each atom. DFT has a history of success in dealing with crystalline and finite systems[119] by calculating the energy of the system through a functional of the electronic

density. The density can be iteratively converged in a self-consistent manner[120], providing a first-principles (ab initio) and parameter-free method that can be applied to all materials. An alternative method to capture the features of a crystal system is the tight-binding approximation, which assumes a reduced basis of tightly bound electronic orbitals. Tight binding is computationally less demanding than DFT but requires parametric models for specific, well-understood systems.

Both approaches allow for accurate calculations of both periodic and finite geometries, and guarantee that physical phenomena at all scales can be included. However, for moiré bilayers with small-lattice mismatch and, thus, large λ_m, the calculations can become demanding.

Commensurate supercells

The starting point for most atomistic models is the construction of a moiré supercell. Atomistic models can only study commensurate systems but allow for the use of Bloch theory and conventional band-structure methods. The most common description of the supercell is with

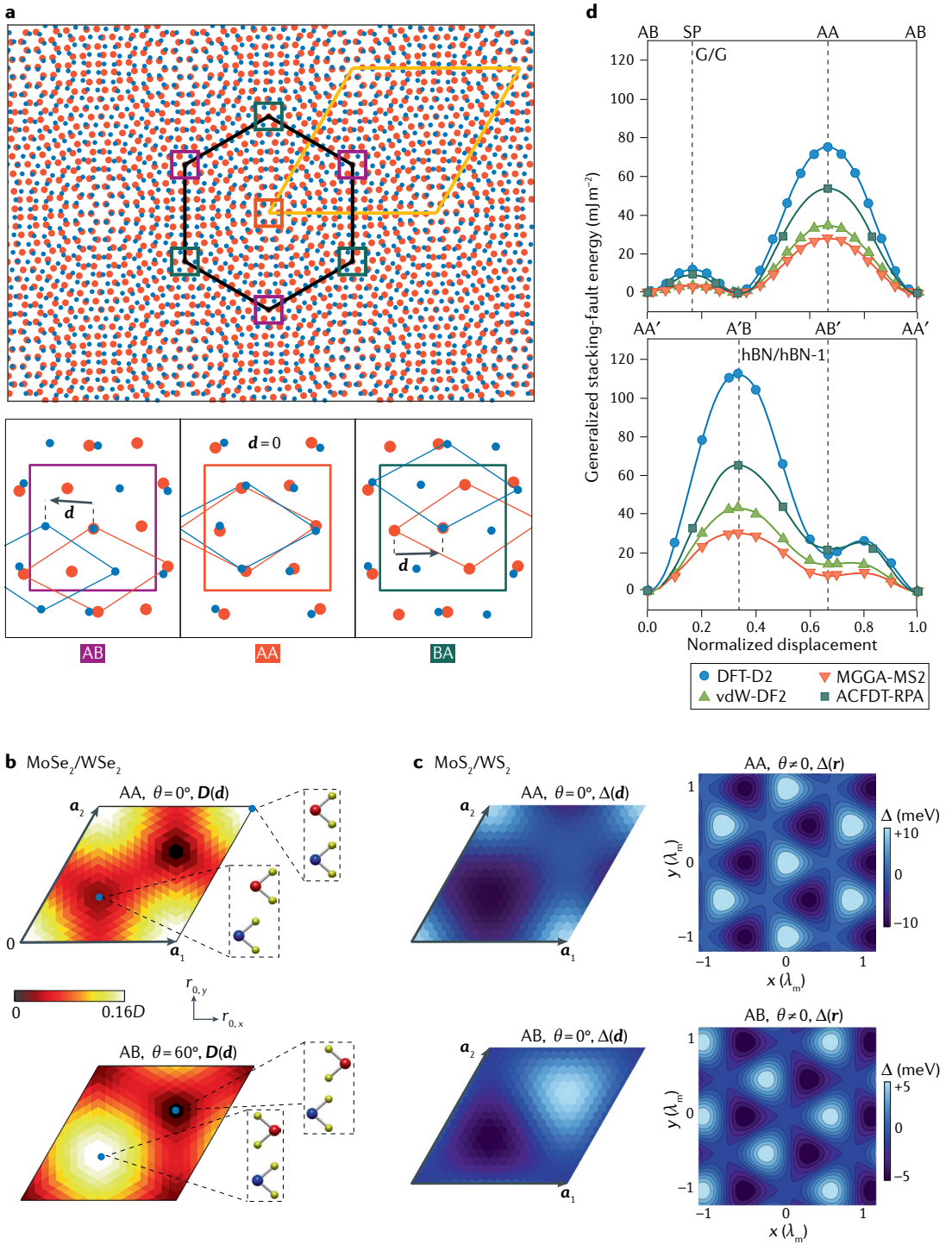

a pair of integers, (M, N), such that one of the superlattice primitive vectors is given by $N\boldsymbol{a}_1 + M\boldsymbol{a}_2$, where $\boldsymbol{a}_i$ are the Bravais lattice vectors of one of the layers. In BOX 1, we provide a simple derivation of this formula for a twisted triangular lattice, although there have been many other derivations specific for the geometry of TBG[41,121–123]. To create twisted moiré superlattices out of heterobilayers with slightly different lattice constants, one can additionally include a small expansion or compression of the layers to help find commensurate supercells[85,86].

Prescriptions for moiré supercells with different geometries are provided in panels **a**–**d** of BOX 1. For arbitrary choices of (M, N), one can obtain supercells whose periodicity is a multiple of the moiré length[123]. This is generally not desirable for small-angle calculations, as it requires many more atoms to be included, so (M, N) should be chosen to ensure that the periodicity is exactly one moiré length. For triangular or square lattices with a small twist angle, this is accomplished with $M = N \pm 1$ (REFS[121,123]), where the sign determines whether the rotation is clockwise or anticlockwise. For a bilayer of rectangular lattices, ensuring $M = \pm 1$ or $N = \pm 1$ suffices[124].

The reciprocal lattice of the supercell, G, can be derived from the supercell lattice vectors, A, with the standard formula $G = 2\pi(A^{\mathrm{T}})^{-1}$. For 2D materials, G and A are 2×2 matrices whose columns correspond to the 2D lattice vectors. The Brillouin zone of the supercell can also be understood in some cases by considering the Brillouin zone of the rotated monolayers. For example, in TBG, the two hexagonal Brillouin zones of the layers can be superimposed with a relative rotation. The line connecting the two original K points (ΔK) forms one edge of the moiré Brillouin zone, and the Γ and M points of the supercell can then be inferred (panel **a** in BOX 2). The Γ point generated in this way usually folds back to the origin via translations of the supercell reciprocal lattice vectors (details of TBG's moiré Brillouin zone in different supercell geometries can be found in the appendix of REF.[123]).

◀ Fig. 3 | **Local stacking order in twisted bilayers. a** | Geometry of a twisted honeycomb bilayer, with the moiré unit cell shown in yellow and the moiré Wigner–Seitz cell in black. Three high-symmetry stacking orders are highlighted in orange, purple and green, corresponding to AA, AB and BA stacking, respectively. Each stacking configuration is defined by a relative displacement between the unit cells of the two lattices, $\boldsymbol{d}$, as shown in the insets. **b** | The optical electric transition dipole moment for an interlayer exciton ($\boldsymbol{D}$) in a $MoSe_2/WSe_2$ heterobilayer, given in units of the dipole moment of an intralayer exciton, D. For transition-metal dichalcogenides, introducing a 60° angle between the layers also changes the atomic geometry, because the two sublattices of the honeycomb lattice are not identical. **c** | The variation as a function of displacement $\boldsymbol{d}$ (left) and position $\boldsymbol{r}$ (right) of the MoS_2 band gap (Δ) within a MoS_2/WS_2 heterobilayer, for AA and AB stacking. This heterostructure can confine electrons and excitons to introduce moiré flat bands. **d** | Generalized stacking-fault energy for a graphene (G) and a hexagonal boron nitride (hBN) bilayer, calculated under different density functional theory van der Waals methods. These data can be used as a starting point for modelling atomic relaxations in twisted bilayers. ACFDT-RPA, adiabatic-connection fluctuation–dissipation theorem with random phase approximation; DFT-D2, density functional with dispersion correction[185]; MGGA-MS2, meta-generalized gradient approximation 'made simple' (REF.[186]); SP, saddle point; vdW-DF2, van der Waals density functional[187]. Panel **b** adapted with permission from REF.[75], APS. Panel **c** adapted with permission from from REF.[78], APS. Panel **d** adapted with permission from REF.[31], APS.

Density functional theory. The most successful computational method for the accurate calculation of atomic and electronic structure in general solid-state systems is DFT[119]. It is a powerful tool in the context of the moiré bilayer problem but has its own limitations. A key constraint is that existing DFT codes rely on periodicity, and, so, only supercell approaches are possible. Electronic structure is obtained completely self-consistently from first principles, but the calculations can become prohibitively expensive for systems containing more than a few hundred atoms. It can also be difficult to draw physical insight from numerical results with only a few selected supercells. Direct DFT calculations of twisted bilayers with large supercells has been performed for many of the common 2D materials, such as graphene[45,125,126], hBN[40], black phosphorus[127] and the TMDCs[63,80]. The numerical complexity can be alleviated by using powerful scaling or parallelization schemes[63,125,127], but these require significant computational resources and expertise. An alternative strategy is to compute unit cells of the untwisted bilayer system but in different stacking arrangements[31,32,63,64,75,82,94,97,99,128]. Electronic and structural information from these reference calculations can be derived and used as input for less computationally intensive models, as described in the section on continuum modelling.

Improvements to basic DFT that are often needed for describing the monolayer physics, such as screening GW corrections, spin–orbit coupling and magnetism, should also be applied to the bilayer. The bilayer geometry is usually defined with the third lattice vector, the c-axis, aligned with $\hat{z}$ and includes a vacuum space of at least 20 Å between periodic images of the 2D heterostructure. The momentum sampling is only needed in two dimensions, as a k-mesh of shape $n \times n \times 1$, as the out-of-plane direction should not include any electronic coupling between periodic images.

In addition, corrections that help capture the van der Waals interactions are often required for accurate prediction of the atomic and electronic structure in 2D bilayers. For 2D crystals, the most important van der Waals force to consider arises from the alignment of temporary dipoles in the electronic wave functions (the London dispersion force), which must be captured by the exchange-correlation functional. There are many choices of corrections to the standard functionals that can help capture van der Waals forces accurately[129]. The methods most relevant for 2D-material modelling directly modify the density functional, and, as such, are named van der Waals density functional (vdW-DF) methods[130]. All modern vdW-DF corrections give reasonable qualitative results for 2D materials, although the exact numbers depend on the functional (FIG. 3d). In practice, the choice is made by considering computational efficiency and availability in the DFT code of choice.

The correlation effects observed in some moiré systems could make the use of DFT approaches inadequate to capture this aspect of the physics. In TBG, the effective Hubbard U parameter, which is a measure of the tendency for correlated behaviour based on on-site electronic repulsion, is small (tens of meV)[131,132], but the minimum predicted energy scale of the twist-induced

moiré flat bands is even smaller at charge neutrality (only a few meV)[96,100,101,126]. The correlations on the moiré superlattice play almost no role at the unit-cell energy scale, and, so, DFT can still provide reliable predictions of the low-energy single-particle electronic structure. To capture the correlated physics, specific mean-field or many-body techniques can then be applied to the obtained single-particle models. For a small sampling of methods applied to TBG, see REFS[133–138]. Often, these approaches rely upon highly reduced tight-binding models for just TBG's flat bands, which are represented as moiré-sized Wannier functions[131,139,140].

Tight-binding models. Instead of dealing with the full electronic density through DFT, for many materials, the electronic structure near the Fermi energy can be reliably reproduced with a tight-binding model that treats the electronic wave function in a localized basis. The tight-binding orbitals can be interpreted in the usual notation for states with definite angular momentum: *s*, *p*, *d*. The single-particle Hamiltonian is then completely described by the couplings between sites, t_{ij}. This Hamiltonian is often written with the basis orbitals in the language of wave functions ($|\phi_i\rangle$) or creation–annihilation operators ($c_i^\dagger, c_i$): $H_{\mathrm{TB}} = \sum_{ij} t_{ij} |\phi_j\rangle\langle\phi_i| = \sum_{ij} t_{ij} c_j^\dagger c_i$. The tight-binding Hamiltonian yields a matrix representation whose elements, the 'hopping terms', are the electronic couplings, $H_{\mathrm{TB}}^{ij} \equiv t_{ij}$, representing the electronic energy for hopping between nearby lattice sites.

Tight-binding models have a much lower computational cost than DFT, usually allowing for calculation of large systems at the cost of self-consistency and ab initio-level accuracy. This general trade-off applies also to models for atomic relaxation that use effective interactions instead of DFT-based forces, such as molecular dynamics with interatomic potentials.

The simplest tight-binding models for TBG have used empirical hopping parameters, often in the context of Slater–Koster theory with parameters fitted from DFT calculations of small-bilayer graphene supercells[122,141–145]. Tight-binding treatments of TBG can access properties of the electronic spectrum beyond simple band structure, such as the Landau levels under magnetic field by way of the Peierls substitution[143,146] and optical responses[11]. They are also convenient for the inclusion of atomic relaxations[96,106,147,148] or defects[118]. More recently, tight-binding approaches have been used for moiré systems beyond TBG, such as multilayer graphene systems[11] or a graphene/TMDC heterobilayer[15].

Ab initio tight-binding models. Even for the simple case of bilayer graphene, the choice of hopping terms can be difficult when using an empirical approach. For example, the interlayer couplings γ_3 and γ_4 of the Slonczewski–Weiss–McClure tight-binding model of graphite[149,150] have the same bonding distance, but, due to the electronic orbitals' orientational dependence, they differ in magnitude by a factor of two[128,151,152]. An approach that combines the virtues of DFT and tight binding is required.

The simplest method refines empirical functionals to better match a reference ab initio band structure[11,153]. A more robust technique avoids band fitting with the construction of maximally localized Wannier functions (MLWF)[154,155]. This approach transforms Bloch eigenstates from a DFT calculation into a set of localized orbitals through a modified Fourier transform that mixes states at each k point. By performing multiple DFT + MLWF calculations for untwisted bilayers of different local stacking orders, a stacking-dependent or spatially dependent interlayer model can be derived without relying on fitting[64,128,151]. The tight-binding models generated in this manner have accuracy similar to that of DFT but carry the computational efficiency of tight binding. This strategy also facilitates an explicit decomposition of the interlayer couplings into symmetry-allowed channels of angular momentum[128], explaining the origin of $\gamma_3 \neq \gamma_4$ in the Slonczewski–Weiss–McClure model. This works well for layers with identical unit cells and, for layers with nearly identical lattices (such as graphene on hBN), one can use artificially imposed strain to create a single unit cell. The intralayer inaccuracy can be tuned depending on the application by choosing to distribute the strain in one layer or evenly between the layers.

For heterobilayers with unit cells that have very different lattice sizes (such as graphene on MoS_2), a more elaborate procedure is required. The simplest solution is to use commensurate supercells. For example, a 3×3 supercell of MoS_2 on a 4×4 supercell of graphene results in a MoS_2/graphene interface with minimal strain. Another possibility involves the storage of monolayer Wannier orbitals to calculate interlayer couplings without an explicit bilayer DFT calculation[156,157]. There are also flake-on-bulk approximations, in which a circular cut-out is taken of one layer and placed on top of a periodic supercell of the other. Electronic properties can then be converged with increasing size[14] or the MLWF technique can be applied to obtain interlayer couplings.

Extremely large systems

The commensurate approximation used to construct moiré superlattices can be avoided in the atomistic case by sacrificing periodicity. In doing so, the conventions of Bloch theory are lost and an electronic band structure can no longer be well defined. Hamiltonians defined on a large but finite flake still permit the calculation of physical observables such as the density of states, optical response and transport parameters. As calculations based on a flake geometry have no periodicity, to regain the same accuracy of Bloch theory, the flake radius must be much larger than the moiré length.

For flake calculations and supercells with extremely small angles ($\theta \ll 1°$), a tight-binding model with millions of atoms is required[91,153]. As direct calculation of eigenvectors for large systems is not computationally efficient, non-diagonalization methods for electronic spectral features are used instead. The most common choice is the family of kernel polynomial methods[158], which approximate operators acting on the electronic Hamiltonian (density of states, optical response, conductivity). The kernel polynomial methods rely only on matrix–vector multiplication, so one can store the tight-binding Hamiltonians as sparse matrices for

a larger reduction in memory and processing overhead. Note that, when these methods are applied to supercells, one must still construct Bloch waves and sample the Brillouin zone to ensure proper calculation of the electronic properties. This method has been used for both flake calculations[91] and extremely large supercells of TBG[7,153]. A related technique uses a real-space recursion relation for the electronic Green's function but still relies on a Chebyshev polynomial basis[159].

An alternative approach for small twist angles is to 'simulate' the effective electronic structure by using a smaller supercell with modified electronic hopping parameters[160]. Such a strategy relies on an existing understanding of how the rotation affects interlayer and intralayer electronic coupling[3].

Continuum modelling

Continuum models for relaxation

For 2D materials with large moiré length, atomic relaxations are important. Relaxations can be treated with standard approaches (molecular dynamics, DFT) already introduced for atomistic electronic-structure

Box 1 | Generating a commensurate moiré geometry

Although the twist angle breaks the translation symmetry of the unit cell, there are special values that create periodic supercells with a translation symmetry of the moiré length. The construction of a commensurate moiré supercell from a primitive Bravais lattice requires finding pairs of lattice sites that match exactly under a rotation. Moiré supercells constructed in this manner are referred to as coincidence-site lattices in studies of grain boundaries[188], and the method generalizes to heterobilayers with different lattice constants by including artificial strain[85,86]. If the original lattice has primitive vectors $\boldsymbol{a}_1$ and $\boldsymbol{a}_2$, then we are looking for integer pairs (M, N) and (M', N') satisfying

$$|M\boldsymbol{a}_1 + N\boldsymbol{a}_2| = |M'\boldsymbol{a}_1 + N'\boldsymbol{a}_2|.$$

For lattices where $|\boldsymbol{a}_1| = |\boldsymbol{a}_2|$ (panel **a**), a good choice is $M' = N$, $N' = M$. For rectangular lattices (figure, panel **b**), $M' = M$, $N' = -N$ can be chosen. For a generic monoclinic lattice, construction of commensurate twisted supercells is not guaranteed. By considering the triangle formed by (0, 0), (M, N) and (M', N') and applying the law of cosines, all of the necessary geometric information on the twisted supercell can be derived.

For a triangular lattice (figure, panel **c**), the squared length from (0, 0) to (M, N) or $(M' = N, N' = M)$ is

$$B^2 \equiv a^2M^2 + 2MN\boldsymbol{a}_1 \cdot \boldsymbol{a}_2 + a^2N^2 = a^2(M^2 + MN + N^2).$$

Similarly, the squared length from (M, N) to (N, M) is

$$C^2 \equiv a^2(M-N)^2 + 2(M-N)(N-M)\boldsymbol{a}_1 \cdot \boldsymbol{a}_2 + a^2(N-M)^2 = a^2(M-N)^2$$

The law of cosines gives $B^2 + B^2 - 2B^2 \cos\theta = C^2$ and simplifies to

$$\cos\theta^{(M,N)} = \frac{2B^2 - C^2}{2B^2} = \frac{M^2 + 4NM + N^2}{2(M^2 + NM + N^2)} \quad (4)$$

This gives the first moiré supercell primitive vector, $N\boldsymbol{a}_1 + M\boldsymbol{a}_2 = M\boldsymbol{a}_1' + N\boldsymbol{a}_2'$, where $\boldsymbol{a}_i'$ is a primitive vector of the rotated layer. The resulting supercell for $M = 3$, $N = 2$ (figure, panel **d**) is but one of many possible choices for a commensurate cell (figure, panel **e**). The pair of matched sites chosen in this construction is not unique, as there are six identical pairs generated by the sixfold rotational symmetry of the lattice[123]. This guarantees that the moiré supercell inherits the point-group symmetry of the original unit cell and gives a prescription for generating all primitive vectors of the moiré supercell. For the triangular lattice, one additional vector is $-M\boldsymbol{a}_1 + (M+N)\boldsymbol{a}_2 = -N\boldsymbol{a}_1' + (M+N)\boldsymbol{a}_1'$.

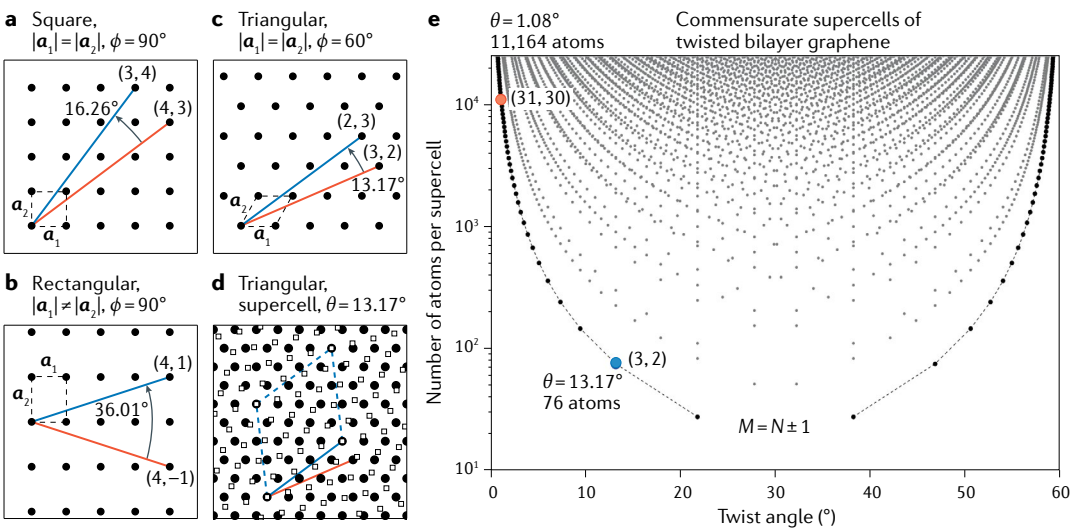

Box 2 | **Bloch-wave expansion for twisted bilayer graphene**

In this example, we focus on twisted bilayer graphene, although the method can be generalized to other materials. We want to construct a Hamiltonian at a given wave vector $\boldsymbol{k}_0$. Without loss of generality, we take $\boldsymbol{k}_0$ near the $\boldsymbol{K}$ point of the first layer's Brillouin zone, K_1 (figure, panel **a**). The central Bloch state in the first layer, $|\psi_1^{\boldsymbol{k}_0}\rangle$, couples to the central state of the second layer, $|\psi_2^{\boldsymbol{k}_0}\rangle$. It also couples to $|\psi_2^{\boldsymbol{k}_0+\boldsymbol{G}_{\boldsymbol{n}}^{L_1}}\rangle$, where $\boldsymbol{G}_{\boldsymbol{n}}^{L_1} = n_1\boldsymbol{G}_1^{L_1} + n_2\boldsymbol{G}_2^{L_1}$ is a reciprocal lattice vector ($\boldsymbol{G}$) of the first layer (L_1). This is because, as Bloch waves, $|\psi_1^{\boldsymbol{k}_0}\rangle$ and $|\psi_1^{\boldsymbol{k}_0+\boldsymbol{G}_{\boldsymbol{n}}^{L_1}}\rangle$ are identical states and represent the same basis element. Repeating this argument with the layer indices reversed, we see that the collection of relevant states for the model is $\{|\psi_1^{\boldsymbol{k}_0+\boldsymbol{G}_{\boldsymbol{m}}^{L_2}}\rangle, |\psi_2^{\boldsymbol{k}_0+\boldsymbol{G}_{\boldsymbol{n}}^{L_1}}\rangle\}$ (figure, panel **b**). This means that the wave vectors of the red layer in the figure inherit the blue layer's reciprocal lattice and vice versa.

The interlayer coupling between Bloch states can be computed by Fourier transforming a hopping functional[98,189], directly projecting from a tight-binding model[100,102] or fitting the stacking dependence of density functional theory band structures[78,99]. We apply the first method and consider the interlayer coupling between a Bloch wave of orbital α on the first layer with that of β on the second,

$$t_{\boldsymbol{G}_n,\boldsymbol{G}_m} = \langle \psi_{2\beta}^{\boldsymbol{k}_0+\boldsymbol{G}_{\boldsymbol{n}}^{L_1}} | H_{21} | \psi_{1\alpha}^{\boldsymbol{k}_0+\boldsymbol{G}_{\boldsymbol{m}}^{L_2}} \rangle$$

where H_{21} is defined by a spatially dependent interlayer coupling $t(\boldsymbol{r})$, and for simplicity we assume that each wave has an orbital sitting at the origin of the twisted bilayer. A subtle point is that the gauge choice for the Bloch phase factor will affect the final form of the interlayer coupling. To later utilize graphene's Dirac Hamiltonian, the Bloch phases must depend only on the lattice position and not the specific position of each orbital[152]. Then, summing over all lattice points in both layers gives

$$t_{\boldsymbol{G}_n,\boldsymbol{G}_m} = \frac{1}{N}\sum_{\boldsymbol{R}_1,\boldsymbol{R}_2} e^{-i(\boldsymbol{k}_0+\boldsymbol{G}_{\boldsymbol{n}}^{L_1})\boldsymbol{R}_2} t(\boldsymbol{R}_2-\boldsymbol{R}_1) e^{i(\boldsymbol{k}_0+\boldsymbol{G}_{\boldsymbol{m}}^{L_2})\boldsymbol{R}_1}$$

$$= \frac{1}{N}\sum_{\boldsymbol{R}_1,\boldsymbol{R}_2} e^{i(\boldsymbol{k}_0+\boldsymbol{G}_{\boldsymbol{m}}^{L_2})\boldsymbol{R}_1 - i(\boldsymbol{k}_0+\boldsymbol{G}_{\boldsymbol{n}}^{L_1})\boldsymbol{R}_2} \int \frac{d\boldsymbol{\xi}}{(2\pi)^2} e^{i\boldsymbol{\xi}(\boldsymbol{R}_2-\boldsymbol{R}_1)} \tilde{t}(\boldsymbol{\xi})$$

$$= \frac{1}{N}\int \frac{d\boldsymbol{\xi}}{(2\pi)^2} \tilde{t}(\boldsymbol{\xi}) \sum_{\boldsymbol{R}_1} e^{i(\boldsymbol{k}_0+\boldsymbol{G}_{\boldsymbol{m}}^{L_2}-\boldsymbol{\xi})\boldsymbol{R}_1} \sum_{\boldsymbol{R}_2} e^{-i(\boldsymbol{k}_0+\boldsymbol{G}_{\boldsymbol{n}}^{L_1}-\boldsymbol{\xi})\boldsymbol{R}_2}$$

where the normalization of both $|\psi\rangle$ introduces N, the number of lattice sites in one layer. The sums are zero unless the momentum argument of the exponent is a reciprocal lattice vector of that layer, in which case, they act like δ-functions. This is only true for both sums when $\boldsymbol{\xi} = \boldsymbol{k}_0 + \boldsymbol{G}_{\boldsymbol{m}}^{L_2} + \boldsymbol{G}_{\boldsymbol{n}}^{L_1}$, which can be confirmed by converting one sum into a Dirac comb (introducing a factor of the monolayer Brillouin zone area), evaluating the integral and then using the other sum to remove the factor of $1/N$. The final expression is $t_{\boldsymbol{G}_n,\boldsymbol{G}_m} = \Omega^{-1}\tilde{t}(\boldsymbol{k}_0 + \boldsymbol{G}_{\boldsymbol{n}}^{L_2} + \boldsymbol{G}_{\boldsymbol{m}}^{L_1})$, where Ω is the area of the monolayer unit cell. This coupling between a (red) Bloch state of the first layer and a (blue) Bloch state of the second layer is represented by the dashed black line in the figure, panel **b**. If the two atomic orbitals do not sit exactly at the origin but instead are shifted by τ_α and τ_β, then these displacements must be included into the argument of t (but remember, not the Bloch phases). This introduces a phase factor of $\exp[i(\boldsymbol{k}_0 + \boldsymbol{G}_{\boldsymbol{n}}^{L_2} + \boldsymbol{G}_{\boldsymbol{m}}^{L_1})(\boldsymbol{\tau}_\beta - \boldsymbol{\tau}_\alpha)]$ to the final expression.

The basic continuum model consists of two ingredients, the intralayer Bloch Hamiltonians and the interlayer coupling, which depends on $\tilde{t}(\boldsymbol{k})$. For twisted bilayer graphene, the Bloch Hamiltonians are often taken to be a Dirac spinor Hamiltonian, $H_D(\boldsymbol{k}) = v_F\boldsymbol{\sigma}\cdot\boldsymbol{k}$, where $\boldsymbol{\sigma}$ is the vector form of the Pauli matrices and v_F is the Fermi velocity. To apply this monolayer Hamiltonian, it is necessary to fold the momenta close to the monolayer $\boldsymbol{K}_i$ points (panel **c**) and take their distance relative to those points in expressing H_D (REF.[3]) (figure, panel **d**). The folded momenta yield a regular hexagonal lattice (panel **e**) that allows for easy interpretation of the relative strength of interlayer couplings: the closer a pair of red and blue Bloch waves, the stronger their coupling. Figure, panel **a** adapted from REF.[1], Springer Nature Limited.

a Moiré Brillouin zone for a twisted supercell

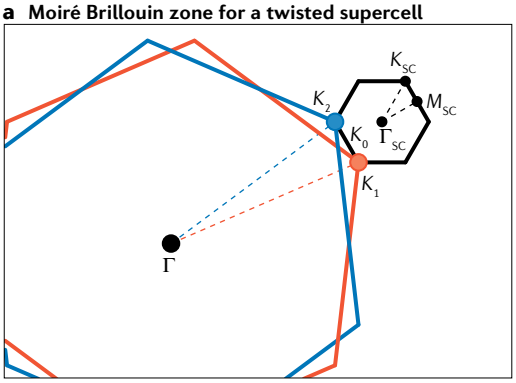

b Generate coupled states

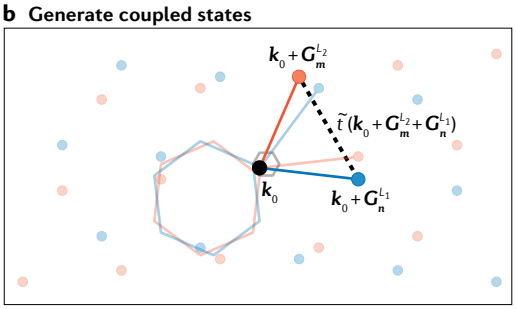

c Fold towards K_i

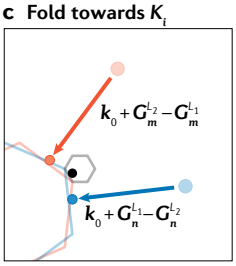

d Take distance from K_i

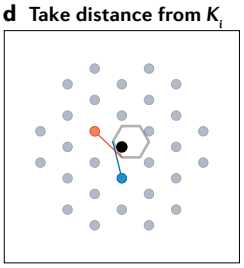

e Continuum model

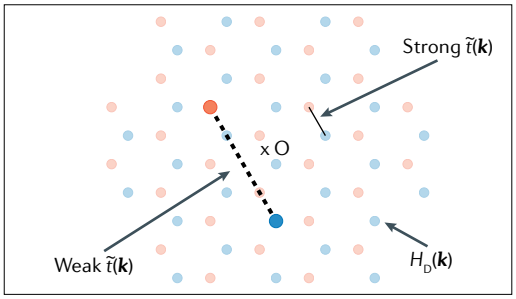

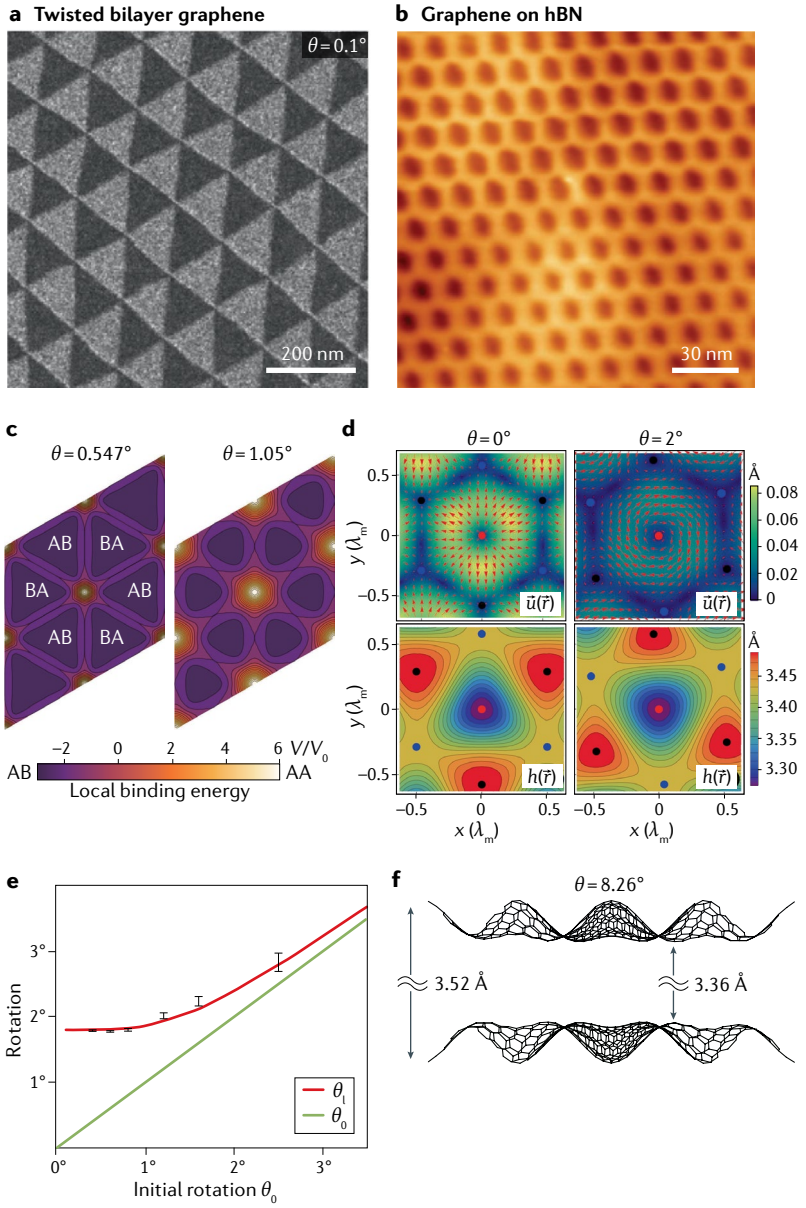

Fig. 4 | **Examples of atomic relaxations in moiré materials. a** | Dark-field transmission electron microscopy measurements of twisted bilayer graphene (TBG) showing the formation of triangular AB/BA stacking domains. **b** | Scanning tunnelling microscopy image of graphene aligned on hexagonal boron nitride (hBN). The sublattice symmetry breaking in hBN introduces hexagonal domains instead of the triangular ones observed in TBG. **c** | Interlayer stacking energy for two different angles of relaxed TBG, computed with a continuum model. **d** | In-plane displacement vector field (**u**) and interlayer distance (*h*) from a continuum model for relaxed graphene on hBN at two different twist angles, in units of the moiré length λ_m. **e** | The local twist at an AA stacking point (θ_l) versus the global twist angle (θ_0) for TBG, computed with a multiscale atomistic model. The saturation of the local twist angle is a consequence of the domain formation. **f** | Vertical corrugation in a supercell of TBG with twist angle 8.26°. Panel **a** adapted from REF.[5], Springer Nature Limited. Panel **b** adapted from REF.[29], Springer Nature Limited. Panel **c** adapted with permission from REF.[96], APS. Panel **d** reprinted with permission from REF.[28], APS. Panel **e** adapted with permission from REF.[169], Elsevier. Panel **f** adapted with permission from REF.[125], APS.

calculations. For molecular-dynamics calculations, many graphene potentials have been fitted to first-principles calculations[161–165]. When the moiré length, λ_m, is on the scale of tens of nanometres, the bilayers often form domains of uniform stacking separated by thin, highly strained transition regions (FIG. 4a,b). These transition regions have an optimal width determined by a balancing of interlayer potential energy and in-plane strain energy[96]. This was first observed in thermally disordered bilayer-graphene samples[4] and in aligned graphene on hBN[29] (FIG. 4b). By controlling the twist angle, regular patterns of AB/BA stacking orders can emerge in graphitic devices[5,29]. The domain-wall networks have their own phonon spectrum[166,167], with the structures vibrating or breathing on the moiré length scale. A continuum model that complements atomistic methods is a powerful approach in modelling these features, which extend across the entire moiré superlattice.

The elastic continuum theory for two interacting layers can be separated into interlayer (out-of-plane) and intralayer (in-plane) energies that depend on the displacement vector field $\boldsymbol{u}(\boldsymbol{r})$. The interlayer energy is usually taken as a generalized stacking-fault energy that depends on the local stacking order between layers[31,94,97,99]. The intralayer energy can assume a linear strain model, which involves gradients of the displacement vector $\partial u_i/\partial r_j \equiv u_{ij}$. The intralayer strain avoids terms of the form $u_{xx} + u_{yy}$, as these represent expansion or compression of the lattice, and, instead, introduces the more energy-favourable shearing terms of the form $u_{xx} - u_{yy}$ and $u_{xy} + u_{yx}$ (REF.[168]) or 'local rotations', $u_{xy} - u_{yx}$, which have no in-plane energy cost. The total energy can then be minimized using any standard numerical optimizer. Typical results from this approach are shown in FIG. 4c,d.

At small twist angles, the layers admit small amounts of in-plane strain to expand regions of low-energy stacking[95–97]. This energy optimization amounts to a local untwisting of the bilayers around the low-energy stacking, which is then compensated by enhanced rotation around the high-energy stacking. In FIG. 4e. we see how the local rotation at the AA spot of TBG saturates below 1° to a constant value, corresponding to a fixed atomic geometry near AA, independent of the twist angle[169]. Thus, although most models for twisted bilayers assume global uniformity in the lattice misalignment, systems with a non-uniform twist angle are more realistic in experimental devices[89]. Simulations that address such non-uniformity have to include straining effects in the electronic structure, and atomic relaxations are important for structures with a large moiré length. Even in a model with a uniform twist angle, global shearing can lower the total energy and modify the electronic structure[148].

Atomic relaxations help explain the band gap observed in graphene/hBN devices[27,28]. In TBG, the sizes of the electronic gaps near the flat bands at the magic angle are underestimated in calculations that assume rigid sheets. The inclusion of relaxation, particularly vertical corrugation (FIG. 4f), modifies the electronic coupling differently at the AA and AB stacking sites[96,101,102,131], resulting in band gaps in better agreement with experimental observations. This band-gap modification is visible in FIG. 5: FIG. 5c shows the band structure obtained with a model that assumes rigid sheets of graphene in the twisted bilayer, whereas FIG. 5d shows the results obtained including relaxations.

Continuum models for electrons

Instead of directly using tight-binding models, the electronic structure of a twisted bilayer can be calculated in a Bloch-wave basis. Owing to the twist angle, the Bloch states of one layer strongly couple to states in the other layer at different momenta, leading to a uniform network of interlayer couplings over an expanded set of Bloch states and forming a momentum lattice. This technique works best when the monolayer band structures are highly dispersive relative to the interlayer coupling in the desired energy region. Then, Bloch states at larger energies enter the low-energy theory perturbatively. The momentum lattice can be truncated efficiently without distorting the desired region of the electronic spectrum, making calculations both accurate and fast. In the case of TBG, the large Fermi velocity of the Dirac cones relative to the interlayer coupling strength means only tens of Bloch waves are needed near $\theta = 1°$.

The continuum expansion was first applied in 2007 in a study of TBG[41]. This was followed by a number of works that more closely analysed the symmetry inherent in this system at large angles[121], the electronic structure at small angles[3,170] and the effects of magnetic fields[146,171,172].

Empirical models. As we have seen, the Hamiltonian of a generic bilayer material consists of two monolayer Hamiltonians, H_1 and H_2, and an interlayer coupling between them, T. We have already investigated the difficulties associated with solving this problem in a tight-binding basis, as the number of orbitals grows with decreasing twist angle. In the electronic continuum model, we expand the bilayer in momentum space, introducing block-diagonal entries $H_1(\boldsymbol{k})$ and $H_2(\boldsymbol{k})$, which are the conventional Bloch Hamiltonians of each 2D layer. Because of the twist angle, the interlayer coupling between the Bloch states depends on the position, $T(\boldsymbol{r})$ and is only periodic on the moiré length scale. T is related to the interlayer orbital couplings, $t(\Delta\boldsymbol{r})$, which are dependent on the relative displacement between atoms ($\Delta\boldsymbol{r}$). Depending on the local configuration $\boldsymbol{d}$, $\Delta\boldsymbol{r}$ changes, modifying t and the effective interlayer coupling H_{21}. T can then be rigorously defined as the local interlayer coupling in terms of the atomic interlayer couplings: $T(\boldsymbol{r}) = \langle \psi_2^{\boldsymbol{k}_2} | H_{21}(\boldsymbol{d}(\boldsymbol{r})) | \psi_1^{\boldsymbol{k}_1} \rangle$ where $\psi_i^{\boldsymbol{k}_i}$ is a Bloch wave of layer i and $\boldsymbol{k}_1$ is not necessarily equal to $\boldsymbol{k}_2$ (see BOX 2 for details). Independent of its derivation, $T(\boldsymbol{r})$ breaks the unit cell translational symmetry in H_1, H_2 and introduces couplings between Bloch states of different momenta on each layer. The resulting Hamiltonian is

$$H(\boldsymbol{k}) = \begin{pmatrix} H_1(\boldsymbol{k}) & T(\boldsymbol{r}) \\ T^{\dagger}(\boldsymbol{r}) & H_2(\boldsymbol{k}) \end{pmatrix} \tag{2}$$

where the mixed basis, $\boldsymbol{k}$ and $\boldsymbol{r}$, reminds us that the momentum-scattering process introduced by the interlayer coupling must still be carefully expanded. We provide a derivation of this expansion in BOX 2. where $\boldsymbol{r}$ is integrated out, leaving a pure $\boldsymbol{k}$ basis for H.

For TBG, spin symmetry is often assumed, so the H_i are 2×2 matrices representing the two p_z orbitals of a single unit cell of graphene. T is expanded in momentum as T_{kp}, to describe the hopping of a Bloch state of momentum p of one layer to momentum k of the other. This scattering process can be indexed by the momenta difference $q_j = p - k$ and, generally, the q_j with smallest magnitude are the most important. The scattering matrices for these smallest q_j take the form

$$T_{kp} \equiv T_j = \begin{pmatrix} w_0 e^{i\phi_j^a} & w_1 e^{i\phi_j^b} \\ w_1 e^{i\phi_j^c} & w_0 e^{i\phi_j^d} \end{pmatrix} \tag{3}$$

where w_0 and w_1 represent interlayer coupling between AA and AB orbital pairs, respectively, and the ϕ_j^i phase factors depend on the orbital positions and choice of origin (see BOX 2 for details). Often, explicit valley symmetry is imposed by assuming no effective coupling at low energy between the K and K' Dirac cones of the monolayer, allowing for $H(\boldsymbol{k})$ to be expanded around a single valley. Combined with the spin symmetry, this results in the eight electrons of magic-angle TBG's flat bands becoming just two bands in the resulting Hamiltonian. One of the most common models, introduced by Bistritzer and MacDonald[3], picks simple Dirac cones for H_i and expands T to only the first Fourier component (corresponding to the three smallest q_j). Also, it assumes that the two layers are perfectly rigid to fix $w_0 = w_1 = 110$ meV. This simplified model works well for predicting the magic angle but misses other details of the electronic structure (FIG. 5c). In double-bilayer graphene, which is a bilayer consisting of two rotated Bernal stacked graphene bilayers, the H_i are 4×4 matrices representing AB stacked bilayer graphene and the T matrices, also 4×4, are only non-zero for the orbitals at the twisted interface[50,51]. This concept can be expanded to multilayers of graphene with one twist angle, where all of the graphene sheets are grouped by their twist angle to form large, interconnected layers for the H_i (REFS[54,60]).

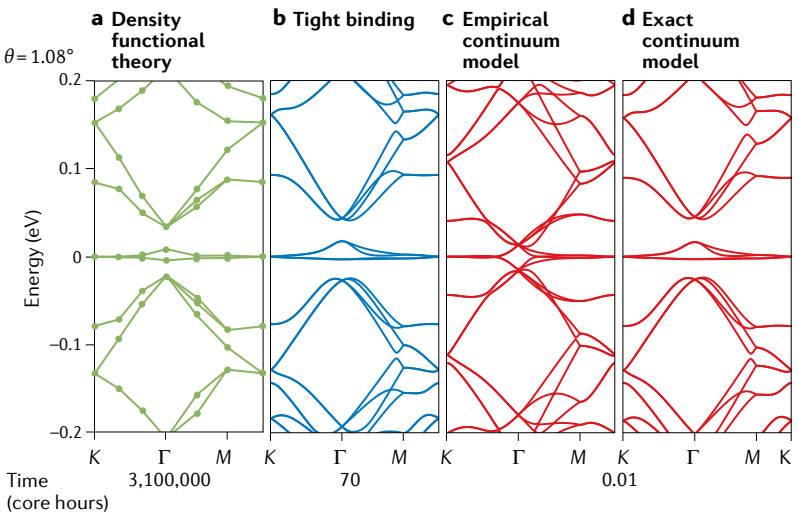

Fig. 5 | **Comparison of electronic band structures for 1.08° twisted bilayer graphene generated by different methods.** The computing time for each method is given in core hours underneath each calculation. **a** | A density functional theory calculation. **b** | A tight-binding calculation[106] using an ab initio tight-binding model[128]. An empirical continuum-model calculation[3] (panel **c**) and an exact continuum-model calculation[101,102] (panel **d**). Panel **a** adapted with permission from REF.[126], APS.

Table 1 | **Summary of the different modelling approaches for moiré heterostructures**

Method	Accuracy	Speed	Ease of use	Choice of material	Choice of angle	Examples of studied materials
DFT with supercells	High	Low	Medium	High	Low	Graphene[125]; hBN[40]; TMDC[80]; other[127]
Molecular dynamics	Medium	Medium	High	Medium	Medium	Graphene[169]; TMDC[94]; other[124]
Elastic continuum	Medium	High	Medium	Medium	High	Graphene[95]; hBN[28]; TMDC[97]
Empirical tight binding	Low	Medium	High	Low	Medium	Graphene[96]
Ab initio tight binding	High	Medium	Medium	Medium	Medium	Graphene[91]; TMDC[64]
Empirical continuum	Low	High	Medium	Low	High	Graphene[3,41]; hBN[26]; TMDC[15]; other[173]
Ab initio continuum	Medium	High	Low	High	High	Graphene[100,101]; hBN[99]; TMDC[81]

We provide a heuristic ranking of each method in different categories. Accuracy considers the likelihood of quantitative agreement with experimental results, whereas speed values low computational cost. Ease of use estimates the amount of domain-specific knowledge needed to employ the model. Choice of material describes how easily the 2D material of interest can be included without significant retooling of the computational approach. Choice of angle evaluates whether the method has any limitations on the twist angle, because of either supercell constraints or computational complexity. DFT, density functional theory; hBN, hexagonal boron nitride; TMDC, transition-metal dichalcogenide.

The extension to trilayer graphene, with two independent twist angles, is more complicated and requires the consideration of additional scattering processes absent in the bilayer case[57,58]. For heterobilayers with greatly different lattice constants, the continuum approach can still apply but requires additional care, as was shown in a study of graphene on $NbSe_2$ (REF.[65]).

The shortcomings of the empirical continuum models can be partly rectified by including atomic relaxations. Vertical corrugations in TBG between the AA and AB stacking sites can be captured by tuning the ratios of the interlayer coupling elements, with $w_0 < w_1$, introducing moiré band gaps that are in better agreement with experiments[131]. If one extends this correction to the limit where the coupling at the AA stacking sites vanishes ($w_0 = 0$), the resulting band structure contains a perfectly flat manifold at the magic angle, with large band gaps on either side[53]. This limit is referred to as the chiral symmetric limit and, building upon earlier perturbative arguments for the vanishing of the Fermi velocity[3], explains the band flattening in TBG in the language of complex analysis. Generic continuum models for arbitrary 2D Bravais lattices show that moiré band flattening can also be anisotropic, which may produce correlated behaviour different to that observed in the isotropic flat bands of TBG[173].

The interlayer coupling in TBG has important implications for the structure of the Landau levels created by magnetic fields[171,172,174]. Analysis of the geometry of TBG supercells reveals two classes of structures: sublattice-exchange even (SE) and sublattice-exchange odd (SO) structures[121–123,171]. SO structures have Landau levels with zero modes[174], whereas the Landau levels in an SE structure are split and have no zero modes[171]. Calculations of graphene on hBN provide additional examples of continuum techniques applied to study the effect of magnetic fields[23,26,30].

Ab initio models. An expansion of the electronic degrees of freedom in reciprocal space can also be performed directly from the band structures of accurate DFT calculations. Similar to the ab initio tight-binding approaches, these continuum models begin with DFT band-structure calculations for untwisted reference cells. By knowing the band structure at different local stackings, one can then approximate the interlayer Bloch-wave coupling over a moiré cell, $T(\boldsymbol{r})$, by studying band gaps or band splitting (FIG. 3c). The Fourier components of this interlayer coupling model are then extracted and can be directly applied to a momentum basis. The role of local stacking on the intralayer Hamiltonian can also be included[81], which is a feature difficult to capture with pure tight-binding approaches.

This technique was first implemented for TBG[99] and graphene on hBN[27,28], and, more recently, has been used for both electrons[79,81] and excitons[78] in TMDCs. Compared with the ab initio tight-binding models, this approach has higher accuracy and is more straightforward to implement. However, as the model extracts band hybridization strengths only from aligned geometries, it can only be applied to small angles, as the full spatial dependence of the interlayer electronic coupling is not captured.

Exact expansions. There are also electronic continuum works that aim to more accurately reproduce the band structures generated by tight-binding models for TBG[100–102,123,151,175]. To do so, the expansion of the electronic structure into Bloch waves is refined by including interlayer and intralayer scattering components out to larger momenta, ensuring that the tight-binding bands are exactly reproduced (FIG. 5d). The details of the low-energy flat bands are highly sensitive to the specific parameterization of the interlayer coupling[100,176]. To capture the electron–hole asymmetry in the low-energy band structure of TBG, the T matrices must depend on the average momenta of the coupled states ($(p+k)/2$), not just their momenta difference ($p-k$) (REFS[100–102]).

Atomic relaxations in TBG at small twist angles lead to the formation of uniform Bernal stacked regions with relatively sharp regions of transitional stackings. Capturing these sharp features necessitates high-frequency Fourier components in reciprocal space in both atomic and electronic continuum models. This greatly increases the strength of interlayer couplings

at higher-momentum shells (larger (q_j))[100,102]. It also reduces the strength of the coupling related to interlayer A-to-A orbital couplings (w_0) even more than expected from vertical corrugation[131], due to a reduction in the size of the AA stacking area[101]. In general, all terms in the exact expansion are dependent on the twist angle, but this dependence is most noticeable for the strongest interlayer coupling term[101,102,123]. Mean-field treatments of electronic screening show that the van Hove singularities in TBG are pinned to the Fermi energy[133], and such corrections can be added to the continuum models[134,177].

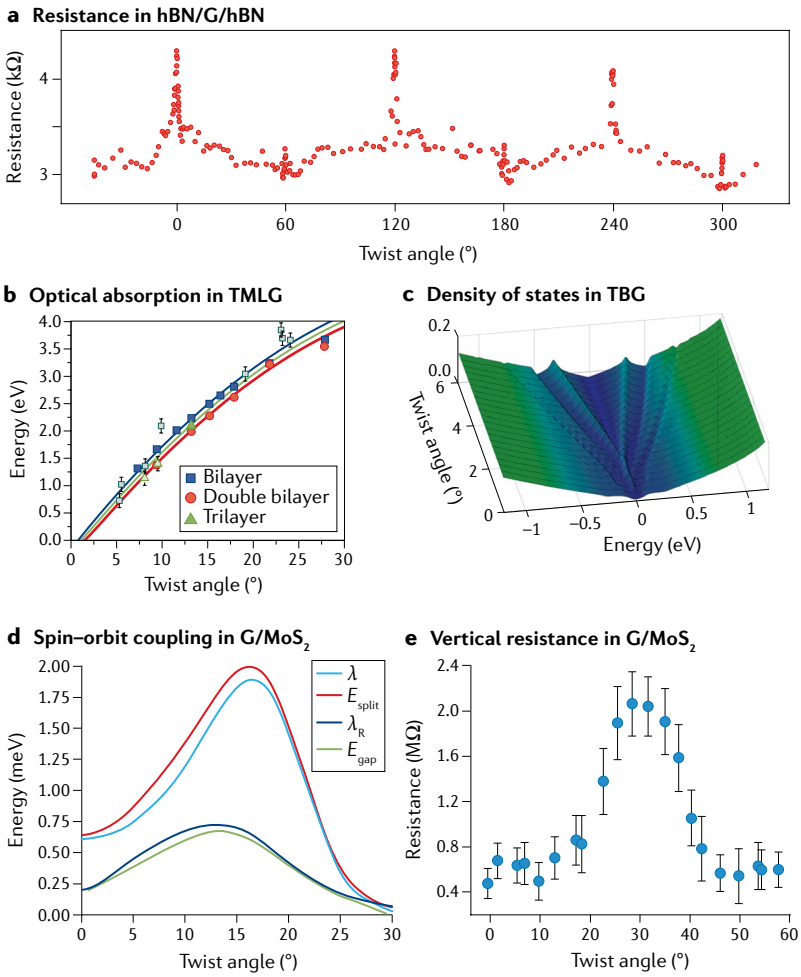

Fig. 6 | **Twist-induced electronic properties in 2D moiré heterostructures.** **a** | Experimentally observed resistivity at charge neutrality (primary Dirac point) from a single device of hexagonal boron nitride (hBN)/graphene (G)/hBN heterostructure, where the twist between the top hBN layer and graphene is controlled in situ. **b** | Energy locations of optical absorption peaks in twisted multilayer graphene (TMLG) caused by van Hove singularities, including density functional theory predictions (filled symbols), experimental values (open symbols) and results from tight-binding calculations (lines), which are in good agreement with the density functional theory predictions. **c** | Electronic density of states for twisted bilayer graphene (TBG) near 0° generated by the finite-flake tight-binding Hamiltonian method. **d** | Twist-angle dependence of the spin–orbit coupling caused by the proximity effect in a heterobilayer of graphene on MoS_2, as obtained from a continuum calculation. λ_R and λ are the values of the effective interlayer electronic coupling and potential, respectively, and E_{gap} and E_{split} are the sizes of the induced moiré band gaps and Dirac point splittings in graphene, respectively. **e** | Vertical conductivity in graphene/MoS_2, as measured by a conductive atomic force microscope, showing an enhancement of the resistance up to a factor of 4 when the layers are maximally misaligned (30°). Panel **a** adapted from REF.[13], Springer Nature Limited. Panel **b** adapted with permission from REF.[11], APS. Panel **c** adapted with permission from REF.[91], APS. Panel **d** adapted with permission from REF.[15], APS. Panel **e** adapted from REF.[10], CC BY 4.0.

Outlook and future directions

A summary of the atomic-structure and electronic-structure methods for moiré heterostructures is provided in TABLE 1. The advantages and disadvantages of each method are described, with a heuristic ranking in five categories. Selected references for each method applied to different bilayer materials are also provided.

In FIG. 5. the different methods for electronic structure are compared for TBG near the magic angle, $\theta = 1.08°$. The DFT, tight-binding and exact continuum models include atomic relaxations and show excellent agreement with one another, in part, because the latter two methods are based on ab initio Wannier tight-binding models. They are also consistent with the experimentally observed moiré band gaps of order 40 meV (REFS[1,2]). The empirical continuum model[3] famously captures the phenomenology of the magic-angle flat bands but fails in many other ways: the band gaps and higher-energy bands are completely different from the experimental ones. As discussed earlier, this is primarily due to the assumption of rigid layers[96,101,131], highlighting the importance of combining electronic and atomic modelling when studying twisted bilayers. For this reason, it is challenging to generate a reliable empirical continuum model for a new material without some preliminary ab initio or experimental input. In terms of computational cost, the continuum models have negligible computational cost, the tight-binding calculations take a few hours on a dedicated few-node machine and DFT approaches take a month on a large computing cluster, despite having a smaller number of sampled k points[125,126].

To conclude, we provide a short summary of recent discoveries in twisted 2D materials as inspiration for future research. A combination of experimentally observed and theoretically predicted twist-dependent electron properties is shown in FIG. 6. Experimental in situ control of the twist angle between a layer of hBN and graphene enabled the measurement of the twist-angle dependence of the resistance at graphene's charge neutrality point[13] (primary Dirac point, FIG. 6a). The peaks in resistance near 0° ± 120° are related to the size of the gap induced in graphene by the sublattice asymmetry in hBN. The optical properties of twisted multilayers of graphene are similarly sensitive to the twist angle, as shown in FIG. 6b. Peaks in the optical absorption are predicted in the DFT calculation and are explained by the emergence of van Hove singularities where the rotated Dirac cones of graphene intersect in momentum space[11]. The exact energy of these peaks can be further tuned by changing the number of layers. The smooth twist-angle dependence of the van Hove singularities can be more clearly seen in finite-flake calculations of the density of states in TBG (FIG. 6c). This method allows for smooth variations of the twist angle free of commensuration conditions[91], and the results are in good agreement with scanning tunnelling microscopy measurements taken at charge neutrality[178].

Spin–orbit coupling or magnetism can be introduced in materials through the proximity effect and tuned by manipulating the twist angle[14–17]. FIGURE 6d shows the results obtained with a continuum model used to study how the interlayer electronic coupling and potential for a graphene/MoS_2 structure depend sensitively on the twist angle, opening up a spin-polarized gap and introducing a spin splitting in the graphene bands[15]. This spin–orbit effect has not been directly observed, but an experimental study of vertical conductivity showed that the electric resistivity in this heterostructure is highly sensitive to the twist angle[10] (FIG. 6e). Graphene/TMDC heterostructures combine the high mobility of graphene with the large symmetry-breaking terms of TMDCs and are, thus, promising candidates for spin-polarized (spintronic) or valley-polarized (valleytronic) technologies.

The most hotly debated issue in the physics of twisted bilayers is the origin of correlated states in moiré flat bands. As more experimental results are reported, examples are emerging in which the superconducting and Mott states in magic-angle TBG do not occur together[179–181], weakening the popular analogy made between superconductivity in TBG and the high-temperature superconductivity in cuprates. There is evidence that the correlated states can break valley, spin and rotational symmetry[182,183], further complicating the phase diagram of magic-angle TBG. Regardless, moiré band flattening (and, hopefully, electronic correlations) should be observable in a wide range of 2D materials, because their driving force — electronic confinement at the extrema of the spatially dependent interlayer coupling $T(\boldsymbol{r})$ — is material-independent. For example, possible superconducting and Mott insulator phases were recently observed in a twisted bilayer of WSe_2 (REF.[184]).

Looking beyond enhanced correlations, other electronic phases can be engineered into moiré bilayers. In TBG, applying a strong vertical electric displacement field when $\theta < 0.5°$ can create a network of topologically protected edge states[6–9]. A simplified interpretation suggests that two symmetry-related stacking orders (AB and BA) are distinguished by the vertical field, opening a band gap of opposite sign in the two regions. The search for other symmetry-breaking perturbations in moiré heterostructures may lead to the discovery of additional platforms for studying topologically protected electronic networks. Other interesting topics include high-quality quasicrystals[55,56], vortex–antivortex networks[4,5] and twist-angle control of excitonic states[76–78]. The controllable design of twisted heterostructures allows for new physics and engineering directions. In this endeavour, theoretical understanding of complicated moiré interfaces will be vital.

Published online 21 July 2020

1. Cao, Y. et al. Correlated insulator behaviour at half-filling in magic-angle graphene superlattices. *Nature* **556**, 80–84 (2018).
2. Cao, Y. et al. Unconventional superconductivity in magic-angle graphene superlattices. *Nature* **556**, 43–50 (2018).
3. Bistritzer, R. & MacDonald, A. H. Moiré bands in twisted double-layer graphene. *Proc. Natl Acad. Sci. USA* **108**, 12233–12237 (2011).
4. Alden, J. S. et al. Strain solitons and topological defects in bilayer graphene. *Proc. Natl Acad. Sci. USA* **110**, 11256–11260 (2013).
5. Yoo, H. et al. Atomic and electronic reconstruction at the van der Waals interface in twisted bilayer graphene. *Nat. Mater.* **18**, 448–453 (2019).
6. San-Jose, P. & Prada, E. Helical networks in twisted bilayer graphene under interlayer bias. *Phys. Rev. B* **88**, 121408 (2013).
7. Ramires, A. & Lado, J. L. Electrically tunable gauge fields in tiny-angle twisted bilayer graphene. *Phys. Rev. Lett.* **121**, 146801 (2018).
8. Huang, S. et al. Topologically protected helical states in minimally twisted bilayer graphene. *Phys. Rev. Lett.* **121**, 037702 (2018).
9. Efimkin, D. K. & MacDonald, A. H. Helical network model for twisted bilayer graphene. *Phys. Rev. B* **98**, 035404 (2018).
10. Liao, M. et al. Twist angle-dependent conductivities across MoS_2/graphene heterojunctions. *Nat. Commun.* **9**, 4068 (2018).
11. Vela, A., Moutinho, M. V. O., Culchac, F. J., Venezuela, P. & Capaz., R. B. Electronic structure and optical properties of twisted multilayer graphene. *Phys. Rev. B* **98**, 155135 (2018).
12. Ribeiro-Palau, R. et al. Twistable electronics with dynamically rotatable heterostructures. *Science* **361**, 690–693 (2018).
13. Finney, N. R. et al. Tunable crystal symmetry in graphene–boron nitride heterostructures with coexisting moiré superlattices. *Nat. Nanotechnol.* **14**, 1029–1034 (2019).
14. Gerber, E., Yao, Y., Arias, T. A. & Kim, E.-A. Ab initio mismatched interface theory of graphene on α–$RuCl_3$: Doping and magnetism. *Phys. Rev. Lett.* **124**, 106804 (2020).
15. Li, Y. & Koshino, M. Twist-angle dependence of the proximity spin-orbit coupling in graphene on transition-metal dichalcogenides. *Phys. Rev. B* **99**, 075438 (2019).
16. David, A., Rakyta, P., Kormányos, A. & Burkard, G. Induced spin-orbit coupling in twisted graphene–transition metal dichalcogenide heterobilayers: twistronics meets spintronics. *Phys. Rev. B* **100**, 085412 (2019).
17. Zollner, K., Faria Junior, P. E. & Fabian, J. Proximity exchange effects in $MoSe_2$ and WSe_2 heterostructures with CrI_3: twist angle, layer, and gate dependence. *Phys. Rev. B* **100**, 085128 (2019).
18. Cheon, G. et al. Data mining for new two- and one-dimensional weakly bonded solids and lattice-commensurate heterostructures. *Nano Lett.* **17**, 1915–1923 (2017).
19. Mounet, N. et al. Two-dimensional materials from high-throughput computational exfoliation of experimentally known compounds. *Nat. Nanotechnol.* **13**, 246–252 (2018).
20. Haastrup, S. et al. The computational 2D materials database: high-throughput modeling and discovery of atomically thin crystals. *2D Mater.* **5**, 042002 (2018).
21. Kindermann, M., Uchoa, B. & Miller, D. L. Zero-energy modes and gate-tunable gap in graphene on hexagonal boron nitride. *Phys. Rev. B* **86**, 115415 (2012).
22. Yankowitz, M. et al. Emergence of superlattice Dirac points in graphene on hexagonal boron nitride. *Nat. Phys.* **8**, 382–386 (2012).
23. Wallbank, J. R., Patel, A. A., Mucha-Kruczyński, M., Geim, A. K. & Fal'ko., V. I. Generic miniband structure of graphene on a hexagonal substrate. *Phys. Rev. B* **87**, 245408 (2013).
24. Mucha-Kruczyński, M., Wallbank, J. R. & Fal'ko, V. I. Heterostructures of bilayer graphene and *h*-BN: Interplay between misalignment, interlayer asymmetry, and trigonal warping. *Phys. Rev. B* **88**, 205418 (2013).
25. Moon, P. & Koshino, M. Electronic properties of graphene/hexagonal-boron-nitride moiré superlattice. *Phys. Rev. B* **90**, 155406 (2014).
26. Song, J. C. W., Samutpraphoot, P. & Levitov, L. S. Topological Bloch bands in graphene superlattices. *Proc. Natl Acad. Sci. USA* **112**, 10879–10883 (2015).
27. Jung, J., DaSilva, A. M., MacDonald, A. H. & Adam, S. Origin of band gaps in graphene on hexagonal boron nitride. *Nat. Commun.* **6**, 6308 (2015).
28. Jung, J., Laksono, E., DaSilva, A. M., MacDonald, A. H. & Mucha-Kruczyński, M. Moiré band model and band gaps of graphene on hexagonal boron nitride. *Phys. Rev. B* **96**, 085442 (2017).
29. Woods, C. R. et al. Commensurate–incommensurate transition in graphene on hexagonal boron nitride. *Nat. Phys.* **10**, 451–456 (2014).
30. Chen, X. et al. Dirac edges of fractal magnetic minibands in graphene with hexagonal moiré superlattices. *Phys. Rev. B* **89**, 075401 (2014).
31. Zhou, S., Han, J., Dai, S., Sun, J. & Srolovitz, D. J. van der Waals bilayer energetics: Generalized stacking-fault energy of graphene, boron nitride, and graphene/boron nitride bilayers. *Phys. Rev. B* **92**, 155438 (2015).
32. Shirodkar, S. N. & Kaxiras, E. Li intercalation at graphene/hexagonal boron nitride interfaces. *Phys. Rev. B* **93**, 245438 (2016).
33. Hunt, B. et al. Massive Dirac fermions and Hofstadter butterfly in a van der Waals heterostructure. *Science* **340**, 1427–1430 (2013).
34. Dean, C. R. et al. Hofstadter's butterfly and the fractal quantum Hall effect in moiré superlattices. *Nature* **497**, 598–602 (2013).
35. Ponomarenko, L. A. et al. Cloning of Dirac fermions in graphene superlattices. *Nature* **497**, 594–597 (2013).
36. Hofstadter, D. R. Energy levels and wave functions of Bloch electrons in rational and irrational magnetic fields. *Phys. Rev. B* **14**, 2239–2249 (1976).
37. Chen, G. et al. Evidence of a gate-tunable Mott insulator in a trilayer graphene moiré superlattice. *Nat. Phys.* **15**, 237–241 (2019).
38. Chen, G. et al. Signatures of tunable superconductivity in a trilayer graphene moiré superlattice. *Nature* **572**, 215–219 (2019).
39. Wang, L. et al. New generation of moiré superlattices in doubly aligned hBN/graphene/hBN heterostructures. *Nano Lett.* **19**, 2371–2376 (2019).
40. Xian, L., Kennes, D. M., Tancogne-Dejean, N., Altarelli, M. & Rubio, A. Multiflat bands and strong correlations in twisted bilayer boron nitride: doping-induced correlated insulator and superconductor. *Nano Lett.* **19**, 4934–4940 (2019).
41. Lopes dos Santos, J. M. B., Peres, N. M. R. & Castro Neto, A. H. Graphene bilayer with a twist: Electronic structure. *Phys. Rev. Lett.* **99**, 256802 (2007).
42. Campanera, J. M., Savini, G., Suarez-Martinez, I. & Heggie, M. I. Density functional calculations on the intricacies of moiré patterns on graphite. *Phys. Rev. B* **75**, 235449 (2007).

43. Yankowitz, M. et al. Tuning superconductivity in twisted bilayer graphene. *Science* **363**, 1059–1064 (2019).
44. Suárez Morell, E., Pacheco, M., Chico, L. & Brey, L. Electronic properties of twisted trilayer graphene. *Phys. Rev. B* **87**, 125414 (2013).
45. Correa, J. D., Pacheco, M. & Morell, E. S. Optical absorption spectrum of rotated trilayer graphene. *J. Mater. Sci.* **49**, 642–647 (2014).
46. Shen, C. et al. Correlated states in twisted double bilayer graphene. *Nat. Phys.* **16**, 520–525 (2020).
47. Liu, X. et al. Spin-polarized correlated insulator and superconductor in twisted double bilayer graphene. Preprint at *arXiv* http://arxiv.org/abs/1903.08130 (2019).
48. Cao, Y. et al. Electric field tunable correlated states and magnetic phase transitions in twisted bilayer-bilayer graphene. Preprint at *arXiv* http://arxiv.org/abs/1903.08596 (2019).
49. Lee, J. Y. et al. Theory of correlated insulating behaviour and spin-triplet superconductivity in twisted double bilayer graphene. *Nat. Commun.* **10**, 5333 (2019).
50. Chebrolu, N. R., Chittari, B. L. & Jung, J. Flat bands in twisted double bilayer graphene. *Phys. Rev. B* **99**, 235417 (2019).
51. Koshino, M. Band structure and topological properties of twisted double bilayer graphene. *Phys. Rev. B* **99**, 235406 (2019).
52. Zhang, Y.-H., Mao, D., Cao, Y., Jarillo-Herrero, P. & Senthil, T. Nearly flat Chern bands in moiré superlattices. *Phys. Rev. B* **99**, 075127 (2019).
53. Tarnopolsky, G., Kruchkov, A. J. & Vishwanath, A. Origin of magic angles in twisted bilayer graphene. *Phys. Rev. Lett.* **122**, 106405 (2019).
54. Liu, J., Ma, Z., Gao, J. & Dai, X. Quantum valley Hall effect, orbital magnetism, and anomalous Hall effect in twisted multilayer graphene systems. *Phys. Rev. X* **9**, 031021 (2019).
55. Ahn, S. J. et al. Dirac electrons in a dodecagonal graphene quasicrystal. *Science* **361**, 782–786 (2018).
56. Moon, P., Koshino, M. & Son, Y.-W. Quasicrystalline electronic states in 30° rotated twisted bilayer graphene. *Phys. Rev. B* **99**, 165430 (2019).
57. Amorim, B. & Castro, E. V. Electronic spectral properties of incommensurate twisted trilayer graphene. Preprint at *arXiv* http://arxiv.org/abs/1807.11909 (2018).
58. Mora, C., Regnault, N. & Bernevig, B. A. Flatbands and perfect metal in trilayer moiré graphene. *Phys. Rev. Lett.* **123**, 026402 (2019).
59. Zuo, W.-J. et al. Scanning tunneling microscopy and spectroscopy of twisted trilayer graphene. *Phys. Rev. B* **97**, 035440 (2018).
60. Khalaf, E., Kruchkov, A. J., Tarnopolsky, G. & Vishwanath, A. Magic angle hierarchy in twisted graphene multilayers. *Phys. Rev. B* **100**, 085109 (2019).
61. Carr, S. et al. Ultraheavy and ultrarelativistic Dirac quasiparticles in sandwiched graphenes. *Nano Lett.* **20**, 3030–3038 (2020).
62. Cea, T., Walet, N. R. & Guinea, F. Twists and the electronic structure of graphitic materials. *Nano Lett.* **19**, 8683–8689 (2019).
63. Kang, J., Li, J., Li, S.-S., Xia, J.-B. & Wang, L.-W. Electronic structural moiré pattern effects on MoS_2/$MoSe_2$ 2D heterostructures. *Nano Lett.* **13**, 5485–5490 (2013).
64. Fang, S. et al. Ab initio tight-binding Hamiltonian for transition metal dichalcogenides. *Phys. Rev. B* **92**, 205108 (2015).
65. Gani, Y. S., Steinberg, H. & Rossi, E. Superconductivity in twisted graphene $NbSe_2$ heterostructures. *Phys. Rev. B* **99**, 235404 (2019).
66. Wang, Q. H., Kalantar-Zadeh, K., Kis, A., Coleman, J. N. & Strano, M. S. Electronics and optoelectronics of two-dimensional transition metal dichalcogenides. *Nat. Nanotechnol.* **7**, 699–712 (2012).
67. Butler, S. Z. et al. Progress, challenges, and opportunities in two-dimensional materials beyond graphene. *ACS Nano* **7**, 2898–2926 (2013).
68. Ataca, C., Sahin, H. & Ciraci, S. Stable, single-layer MX_2 transition-metal oxides and dichalcogenides in a honeycomb-like structure. *J. Phys. Chem. C* **116**, 8983–8999 (2012).
69. Duerloo, K.-A. N., Li, Y. & Reed, E. J. Structural phase transitions in two-dimensional Mo- and W-dichalcogenide monolayers. *Nat. Commun.* **5**, 4214 (2014).
70. Rasmussen, F. A. & Thygesen, K. S. Computational 2D materials database: electronic structure of transition-metal dichalcogenides and oxides. *J. Phys. Chem. C* **119**, 13169–13183 (2015).
71. Navarro-Moratalla, E. et al. Enhanced superconductivity in atomically thin TaS_2. *Nat. Commun.* **7**, 11043 (2016).
72. Yang, Y. et al. Enhanced superconductivity upon weakening of charge density wave transport in 2*H*–TaS_2 in the two-dimensional limit. *Phys. Rev. B* **98**, 035203 (2018).
73. Liu, K. et al. Evolution of interlayer coupling in twisted molybdenum disulfide bilayers. *Nat. Commun.* **5**, 4966 (2014).
74. Zhang, C. et al. Interlayer couplings, moiré patterns, and 2D electronic superlattices in MoS_2/WSe_2 hetero-bilayers. *Sci. Adv.* **3**, e1601459 (2017).
75. Yu, H., Wang, Y., Tong, Q., Xu, X. & Yao, W. Anomalous light cones and valley optical selection rules of interlayer excitons in twisted heterobilayers. *Phys. Rev. Lett.* **115**, 187002 (2015).
76. Tran, K. et al. Evidence for moiré excitons in van der Waals heterostructures. *Nature* **567**, 71–75 (2019).
77. Jin, C. et al. Observation of moiré excitons in WSe_2/WS_2 heterostructure superlattices. *Nature* **567**, 76–80 (2019).
78. Wu, F., Lovorn, T. & MacDonald, A. H. Topological exciton bands in moiré heterojunctions. *Phys. Rev. Lett.* **118**, 147401 (2017).
79. Wu, F., Lovorn, T., Tutuc, E. & MacDonald, A. H. Hubbard model physics in transition metal dichalcogenide moiré bands. *Phys. Rev. Lett.* **121**, 026402 (2018).
80. Naik, M. H. & Jain, M. Ultraflatbands and shear solitons in moiré patterns of twisted bilayer transition metal dichalcogenides. *Phys. Rev. Lett.* **121**, 266401 (2018).
81. Wu, F., Lovorn, T., Tutuc, E., Martin, I. & MacDonald, A. H. Topological insulators in twisted transition metal dichalcogenide homobilayers. *Phys. Rev. Lett.* **122**, 086402 (2019).
82. Sivadas, N., Okamoto, S., Xu, X., Fennie, C. J. & Xiao, D. Stacking-dependent magnetism in bilayer CrI_3. *Nano Lett.* **18**, 7658–7664 (2018).
83. Jiang, P. et al. Stacking tunable interlayer magnetism in bilayer CrI_3. *Phys. Rev. B* **99**, 144401 (2019).
84. Novoselov, K. S., Mishchenko, A., Carvalho, A. & Castro Neto, A. H. 2D materials and van der Waals heterostructures. *Science* **353**, aac9439 (2016).
85. Lazić, P. CellMatch: Combining two unit cells into a common supercell with minimal strain. *Comput. Phys. Commun.* **197**, 324–334 (2015).
86. Koda, D. S., Bechstedt, F., Marques, M. & Teles, L. K. Coincidence lattices of 2D crystals: Heterostructure predictions and applications. *J. Phys. Chem. C* **120**, 10895–10908 (2016).
87. Frisenda, R. et al. Recent progress in the assembly of nanodevices and van der Waals heterostructures by deterministic placement of 2D materials. *Chem. Soc. Rev.* **47**, 53–68 (2018).
88. Kim, K. et al. van der Waals heterostructures with high accuracy rotational alignment. *Nano Lett.* **16**, 1989–1995 (2016).
89. Uri, A. et al. Mapping the twist-angle disorder and Landau levels in magic-angle graphene. *Nature* **581**, 47–52 (2020).
90. van Wijk, M. M., Schuring, A., Katsnelson, M. I. & Fasolino, A. Relaxation of moiré patterns for slightly misaligned identical lattices: graphene on graphite. *2D Mater.* **2**, 034010 (2015).
91. Carr, S. et al. Twistronics: manipulating the electronic properties of two-dimensional layered structures through their twist angle. *Phys. Rev. B* **95**, 075420 (2017).
92. Massatt, D., Luskin, M. & Ortner, C. Electronic density of states for incommensurate layers. *Multiscale Model. Simul.* **15**, 476–499 (2017).
93. Bernal, J. D. The structure of graphite. *Proc. R. Soc. Lond. A Math. Phys. Sci* **106**, 749–773 (1924).
94. Kumar, H., Er, D., Dong, L., Li, J. & Shenoy, V. B. Elastic deformations in 2D van der Waals heterostructures and their impact on optoelectronic properties: predictions from a multiscale computational approach. *Sci. Rep.* **5**, 10872 (2015).
95. Dai, S., Xiang, Y. & Srolovitz, D. J. Twisted bilayer graphene: Moiré with a twist. *Nano Lett.* **16**, 5923–5927 (2016).
96. Nam, N. N. T. & Koshino, M. Lattice relaxation and energy band modulation in twisted bilayer graphene. *Phys. Rev. B* **96**, 075311 (2017).
97. Carr, S. et al. Relaxation and domain formation in incommensurate two-dimensional heterostructures. *Phys. Rev. B* **98**, 224102 (2018).
98. Bistritzer, R. & MacDonald, A. H. Transport between twisted graphene layers. *Phys. Rev. B* **81**, 245412 (2010).
99. Jung, J., Raoux, A., Qiao, Z. & MacDonald, A. H. Ab initio theory of moiré superlattice bands in layered two-dimensional materials. *Phys. Rev. B* **89**, 205414 (2014).
100. Guinea, F. & Walet, N. R. Continuum models for twisted bilayer graphene: Effect of lattice deformation and hopping parameters. *Phys. Rev. B* **99**, 205134 (2019).
101. Carr, S., Fang, S., Zhu, Z. & Kaxiras, E. Exact continuum model for low-energy electronic states of twisted bilayer graphene. *Phys. Rev. Res.* **1**, 013001 (2019).
102. Fang, S., Carr, S., Zhu, Z., Massatt, D. & Kaxiras, E. Angle-dependent *ab initio* low-energy Hamiltonians for a relaxed twisted bilayer graphene heterostructure. Preprint at *arXiv* https://arxiv.org/abs/1908.00058 (2019).
103. Morsch, O. & Oberthaler, M. Dynamics of Bose-Einstein condensates in optical lattices. *Rev. Mod. Phys.* **78**, 179–215 (2006).
104. Forsythe, C. et al. Band structure engineering of 2D materials using patterned dielectric superlattices. *Nat. Nanotechnol.* **13**, 566–571 (2018).
105. Shi, L., Ma, J. & Song, J. C. W. Gate-tunable flat bands in van der Waals patterned dielectric superlattices. *2D Mater.* **7**, 015028 (2019).
106. Carr, S., Fang, S., Jarillo-Herrero, P. & Kaxiras, E. Pressure dependence of the magic twist angle in graphene superlattices. *Phys. Rev. B* **98**, 085144 (2018).
107. Chittari, B. L., Leconte, N., Javvaji, S. & Jung, J. Pressure induced compression of flatbands in twisted bilayer graphene. *Electron. Struct.* **1**, 015001 (2018).
108. Li, L. J. et al. Controlling many-body states by the electric-field effect in a two-dimensional material. *Nature* **529**, 185–189 (2016).
109. Amorim, B. et al. Novel effects of strains in graphene and other two dimensional materials. *Phys. Rep.* **617**, 1–54 (2016).
110. Naumis, G. G., Barraza-Lopez, S., Oliva-Leyva, M. & Terrones, H. Electronic and optical properties of strained graphene and other strained 2D materials: a review. *Rep. Prog. Phys.* **80**, 096501 (2017).
111. Fang, S., Carr, S., Cazalilla, M. A. & Kaxiras, E. Electronic structure theory of strained two-dimensional materials with hexagonal symmetry. *Phys. Rev. B* **98**, 075106 (2018).
112. Bi, Z., Yuan, N. F. Q. & Fu, L. Designing flat bands by strain. *Phys. Rev. B* **100**, 035448 (2019).
113. Shao, X., Wang, K., Pang, R. & Shi, X. Lithium intercalation in graphene/MoS_2 composites: First-principles insights. *J. Phys. Chem. C* **119**, 25860–25867 (2015).
114. Wan, J. et al. Tuning two-dimensional nanomaterials by intercalation: materials, properties and applications. *Chem. Soc. Rev.* **45**, 6742–6765 (2016).
115. Bediako, D. K. et al. Heterointerface effects in the electrointercalation of van der Waals heterostructures. *Nature* **558**, 425–429 (2018).
116. Larson, D. T., Fampiou, I., Kim, G. & Kaxiras, E. Lithium intercalation in graphene–MoS_2 heterostructures. *J. Phys. Chem. C* **122**, 24535–24541 (2018).
117. Lin, Z. et al. Defect engineering of two-dimensional transition metal dichalcogenides. *2D Mater.* **3**, 022002 (2016).
118. Ramires, A. & Lado, J. L. Impurity-induced triple point fermions in twisted bilayer graphene. *Phys. Rev. B* **99**, 245118 (2019).
119. Jones, R. O. Density functional theory: Its origins, rise to prominence, and future. *Rev. Mod. Phys.* **87**, 897–923 (2015).
120. Hohenberg, P. & Kohn, W. Inhomogeneous electron gas. *Phys. Rev.* **136**, B864–B871 (1964).
121. Mele, E. J. Commensuration and interlayer coherence in twisted bilayer graphene. *Phys. Rev. B* **81**, 161405 (2010).
122. Shallcross, S., Sharma, S., Kandelaki, E. & Pankratov, O. A. Electronic structure of turbostratic graphene. *Phys. Rev. B* **81**, 165105 (2010).
123. Lopes dos Santos, J. M. B., Peres, N. M. R. & Castro Neto, A. H. Continuum model of the twisted graphene bilayer. *Phys. Rev. B* **86**, 155449 (2012).
124. Pan, D., Wang, T.-C., Xiao, W., Hu, D. & Yao, Y. Simulations of twisted bilayer orthorhombic black phosphorus. *Phys. Rev. B* **96**, 041411 (2017).
125. Uchida, K., Furuya, S., Iwata, J.-I. & Oshiyama, A. Atomic corrugation and electron localization due to moiré patterns in twisted bilayer graphenes. *Phys. Rev. B* **90**, 155451 (2014).

126. Lucignano, P., Alfè, D., Cataudella, V., Ninno, D. & Cantele, G. Crucial role of atomic corrugation on the flat bands and energy gaps of twisted bilayer graphene at the magic angle $\theta \sim 1.08°$. *Phys. Rev. B* **99**, 195419 (2019).
127. Kang, P. et al. Moiré impurities in twisted bilayer black phosphorus: effects on the carrier mobility. *Phys. Rev. B* **96**, 195406 (2017).
128. Fang, S. & Kaxiras, E. Electronic structure theory of weakly interacting bilayers. *Phys. Rev. B* **93**, 235153 (2016).
129. Berland, K. et al. van der Waals forces in density functional theory: a review of the vdW-DF method. *Rep. Prog. Phys.* **78**, 066501 (2015).
130. Dion, M., Rydberg, H., Schröder, E., Langreth, D. C. & Lundqvist, B. I. Van der Waals density functional for general geometries. *Phys. Rev. Lett.* **92**, 246401 (2004).
131. Koshino, M. et al. Maximally localized Wannier orbitals and the extended Hubbard model for twisted bilayer graphene. *Phys. Rev. X* **8**, 031087 (2018).
132. Goodwin, Z. A. H., Corsetti, F., Mostofi, A. A. & Lischner, J. Attractive electron-electron interactions from internal screening in magic-angle twisted bilayer graphene. *Phys. Rev. B* **100**, 235424 (2019).
133. Rademaker, L., Abanin, D. A. & Mellado, P. Charge smoothening and band flattening due to Hartree corrections in twisted bilayer graphene. *Phys. Rev. B* **100**, 205114 (2019).
134. Cea, T., Walet, N. R. & Guinea, F. Electronic band structure and pinning of Fermi energy to van Hove singularities in twisted bilayer graphene: a self-consistent approach. *Phys. Rev. B* **100**, 205113 (2019).
135. Roy, B. & Juričić, V. Unconventional superconductivity in nearly flat bands in twisted bilayer graphene. *Phys. Rev. B* **99**, 121407 (2019).
136. Das Sarma, S. & Wu, F. Electron–phonon and electron–electron interaction effects in twisted bilayer graphene. *Ann. Phys.* **417**, 168193 (2020).
137. Wu, F., MacDonald, A. H. & Martin, I. Theory of phonon-mediated superconductivity in twisted bilayer graphene. *Phys. Rev. Lett.* **121**, 257001 (2018).
138. Bultinck, N. et al. Ground state and hidden symmetry of magic angle graphene at even integer filling. Preprint at *arXiv* https://arxiv.org/abs/1911.02045 (2019).
139. Kang, J. & Vafek, O. Symmetry, maximally localized Wannier states, and a low-energy model for twisted bilayer graphene narrow bands. *Phys. Rev. X* **8**, 031088 (2018).
140. Carr, S., Fang, S., Po, H. C., Vishwanath, A. & Kaxiras, E. Derivation of Wannier orbitals and minimal-basis tight-binding Hamiltonians for twisted bilayer graphene: First-principles approach. *Phys. Rev. Res.* **1**, 033072 (2019).
141. Suárez Morell, E., Correa, J. D., Vargas, P., Pacheco, M. & Barticevic, Z. Flat bands in slightly twisted bilayer graphene: tight-binding calculations. *Phys. Rev. B* **82**, 121407 (2010).
142. Trambly de Laissardière, G., Mayou, D. & Magaud, L. Localization of Dirac electrons in rotated graphene bilayers. *Nano Lett.* **10**, 804–808 (2010).
143. Wang, Z. F., Liu, F. & Chou, M. Y. Fractal Landau-level spectra in twisted bilayer graphene. *Nano Lett.* **12**, 3833–3838 (2012).
144. Sboychakov, A. O., Rakhmanov, A. L., Rozhkov, A. V. & Nori, F. Electronic spectrum of twisted bilayer graphene. *Phys. Rev. B* **92**, 075402 (2015).
145. Lin, X. & Tománek, D. Minimum model for the electronic structure of twisted bilayer graphene and related structures. *Phys. Rev. B* **98**, 081410 (2018).
146. Moon, P. & Koshino, M. Energy spectrum and quantum Hall effect in twisted bilayer graphene. *Phys. Rev. B* **85**, 195458 (2012).
147. Gargiulo, F. & Yazyev, O. V. Structural and electronic transformation in low-angle twisted bilayer graphene. *2D Mater.* **5**, 015019 (2017).
148. Lin, X., Liu, D. & Tománek, D. Shear instability in twisted bilayer graphene. *Phys. Rev. B* **98**, 195432 (2018).
149. McClure, J. W. Band structure of graphite and de Haas-van Alphen effect. *Phys. Rev.* **108**, 612–618 (1957).
150. Slonczewski, J. C. & Weiss, P. R. Band structure of graphite. *Phys. Rev.* **109**, 272–279 (1958).
151. Jung, J. & MacDonald, A. H. Accurate tight-binding models for the π bands of bilayer graphene. *Phys. Rev. B* **89**, 035405 (2014).
152. Castro Neto, A. H., Guinea, F., Peres, N. M. R., Novoselov, K. S. & Geim, A. K. The electronic properties of graphene. *Rev. Mod. Phys.* **81**, 109–162 (2009).
153. Trambly de Laissardière, G., Mayou, D. & Magaud, L. Numerical studies of confined states in rotated bilayers of graphene. *Phys. Rev. B* **86**, 125413 (2012).
154. Marzari, N., Mostofi, A. A., Yates, J. R., Souza, I. & Vanderbilt, D. Maximally localized Wannier functions: Theory and applications. *Rev. Mod. Phys.* **84**, 1419–1475 (2012).
155. Pizzi, G. et al. Wannier90 as a community code: new features and applications. *J. Phys. Condens. Matter* **32**, 165902 (2020).
156. Bakhta, A., Cancès, E., Cazeaux, P., Fang, S. & Kaxiras, E. Compression of Wannier functions into Gaussian-type orbitals. *Comput. Phys. Commun.* **230**, 27–37 (2018).
157. Tritsaris, G. A. et al. Perturbation theory for weakly coupled two-dimensional layers. *J. Mater. Res.* **31**, 959–966 (2016).
158. Weiße, A., Wellein, G., Alvermann, A. & Fehske, H. The kernel polynomial method. *Rev. Mod. Phys.* **78**, 275–306 (2006).
159. Le, H. A. & Do, V. N. Electronic structure and optical properties of twisted bilayer graphene calculated via time evolution of states in real space. *Phys. Rev. B* **97**, 125136 (2018).
160. Gonzalez-Arraga, L. A., Lado, J. L., Guinea, F. & San-Jose, P. Electrically controllable magnetism in twisted bilayer graphene. *Phys. Rev. Lett.* **119**, 107201 (2017).
161. Stuart, S. J., Tutein, A. B. & Harrison, J. A. A reactive potential for hydrocarbons with intermolecular interactions. *J. Chem. Phys.* **112**, 6472–6486 (2000).
162. Kolmogorov, A. N. & Crespi, V. H. Registry-dependent interlayer potential for graphitic systems. *Phys. Rev. B* **71**, 235415 (2005).
163. Los, J. H., Ghiringhelli, L. M., Meijer, E. J. & Fasolino, A. Improved long-range reactive bond-order potential for carbon. I. Construction. *Phys. Rev. B* **72**, 214102 (2005).
164. O'Connor, T. C., Andzelm, J. & Robbins, M. O. AIREBO-M: A reactive model for hydrocarbons at extreme pressures. *J. Chem. Phys.* **142**, 024903 (2015).
165. Wen, M., Carr, S., Fang, S., Kaxiras, E. & Tadmor, E. B. Dihedral-angle-corrected registry-dependent interlayer potential for multilayer graphene structures. *Phys. Rev. B* **98**, 235404 (2018).
166. Lin, M.-L. et al. Moiré phonons in twisted bilayer MoS_2. *ACS Nano* **12**, 8770–8780 (2018).
167. Koshino, M. & Son, Y.-W. Moiré phonons in twisted bilayer graphene. *Phys. Rev. B* **100**, 075416 (2019).
168. Gong, X. & Mele, E. J. Stacking textures and singularities in bilayer graphene. *Phys. Rev. B* **89**, 121415 (2014).
169. Zhang, K. & Tadmor, E. B. Structural and electron diffraction scaling of twisted graphene bilayers. *J. Mech. Phys. Solids* **112**, 225–238 (2018).
170. Mele, E. J. Band symmetries and singularities in twisted multilayer graphene. *Phys. Rev. B* **84**, 235439 (2011).
171. Kindermann, M. & Mele, E. J. Landau quantization in twisted bilayer graphene: the Dirac comb. *Phys. Rev. B* **84**, 161406 (2011).
172. Bistritzer, R. & MacDonald, A. H. Moiré butterflies in twisted bilayer graphene. *Phys. Rev. B* **84**, 035440 (2011).
173. Kariyado, T. & Vishwanath, A. Flat band in twisted bilayer Bravais lattices. *Phys. Rev. Res.* **1**, 033076 (2019).
174. de Gail, R., Goerbig, M. O., Guinea, F., Montambaux, G. & Castro Neto, A. H. Topologically protected zero modes in twisted bilayer graphene. *Phys. Rev. B* **84**, 045436 (2011).
175. Shallcross, S., Sharma, S. & Pankratov, O. Emergent momentum scale, localization, and van Hove singularities in the graphene twist bilayer. *Phys. Rev. B* **87**, 245403 (2013).
176. Walet, N. R. & Guinea, F. Lattice deformation, low energy models and flat bands in twisted graphene bilayers. Preprint at *arXiv* http://arxiv.org/abs/1903.00340 (2019).
177. Guinea, F. & Walet, N. R. Electrostatic effects, band distortions, and superconductivity in twisted graphene bilayers. *Proc. Natl Acad. Sci. USA* **115**, 13174–13179 (2018).
178. Brihuega, I. et al. Unraveling the intrinsic and robust nature of van Hove singularities in twisted bilayer graphene by scanning tunneling microscopy and theoretical analysis. *Phys. Rev. Lett.* **109**, 196802 (2012).
179. Stepanov, P. et al. The interplay of insulating and superconducting orders in magic-angle graphene bilayers. Preprint at *arXiv* http://arxiv.org/abs/1911.09198 (2019)
180. Saito, Y. et al. Independent superconductors and correlated insulators in twisted bilayer graphene. *Nat. Phys.* https://doi.org/10.1038/s41567-020-0928-3 (2020).
181. Arora, H. S. et al. Superconductivity without insulating states in twisted bilayer graphene stabilized by monolayer WSe_2. Preprint at *arXiv* http://arxiv.org/abs/2002.03003 (2020).
182. Sharpe, A. L. et al. Emergent ferromagnetism near three-quarters filling in twisted bilayer graphene. *Science* **365**, 605–608 (2019).
183. Jiang, Y. et al. Charge order and broken rotational symmetry in magic-angle twisted bilayer graphene. *Nature* **573**, 91–95 (2019).
184. Wang, L. et al. Magic continuum in twisted bilayer WSe_2. Preprint at arXiv http://arxiv.org/abs/1910.12147 (2019).
185. Grimme, S. Semiempirical GGA-type density functional constructed with a long-range dispersion correction. *J. Comput. Chem.* **27**, 1787–1799 (2006).
186. Sun, J. et al. Semilocal and hybrid meta-generalized gradient approximations based on the understanding of the kinetic-energy-density dependence. *J. Chem. Phys.* **138**, 044113 (2013).
187. Klimeš, J., Bowler, D. R. & Michaelides, A. Chemical accuracy for the van der Waals density functional. *J. Phys. Condens. Matter* **22**, 022201 (2009).
188. Ranganathan, S. On the geometry of coincidence-site lattices. *Acta Crystallogr.* **21**, 197–199 (1966).
189. Koshino, M. Interlayer interaction in general incommensurate atomic layers. *New J. Phys.* **17**, 015014 (2015).

Acknowledgements
The authors thank Z. Zhu, D. Larson and E. Kucukbenli for helpful discussions and reference recommendations. This work was supported in part by ARO MURI award no. W911NF-14-0247 and by the STC Center for Integrated Quantum Materials, NSF grant no. DMR-1231319. The tight-binding calculation shown in Fig. 5 was run on the Odyssey cluster supported by the FAS Division of Science, Research Computing Group at Harvard University.

Author contributions
S.C. designed the figures and all authors contributed to the writing and editing of the manuscript.

Competing interests
The authors declare no competing interests.

Publisher's note
Springer Nature remains neutral with regard to jurisdictional claims in published maps and institutional affiliations.